Deepening the theoretical understanding of vector inversion generators

T. Wens,[1] P. Laurent,[1] J.-F. Fagnard,[1] C. Greffe,[2] and P. Vanderbemden[1]
[1)] *Montefiore institute, University of Liège, 4000 Liège, Belgium*
[2)] *GeneriX srl, 4000 Liège, Belgium*

(*Electronic mail: twens@uliege.be)

(Dated: 10 August 2023)

Vector inversion generators, or spiral generators, are compact, high voltage pulse generators consisting of a pair of conducting foils wound in a spiral and a switch. We developed an improved analytical model predicting the time evolution of the output voltage of such spiral generators. Our model (i) takes into account that the current in the switch results from the current on the active and passive waveguides and (ii) takes into account the losses of the conductor in the equations describing the propagation of the voltage and current pulses in both waveguides. The model is compared to experimental results involving different input switches and at different temperatures to investigate the influence of resistive losses on the output voltage. The model is further developed to obtain the time evolution of the current in the switch. Our model is then used to predict the amplitude of the first two peaks of the oscillatory response of spiral generators as a function of a set of dimensionless parameters.

I. INTRODUCTION

The generation of short high voltage pulses (tens to hundreds of kilovolts with a rise time ranging from nanoseconds to microseconds) is of considerable interest for a range of engineering applications including rock fracturing[1], food sterilization without alteration of the nutrition[2] or as trigger generator for other devices, for example as input voltage of X-ray tubes[3] or to improve the switching performance of thyristors[4]. Several technologies are available to generate high voltage pulses, such as Marx generators[5–7] or Blumlein generators[8–11]. For applications in which compact, lightweight voltage generators are required, spiral generators are strong candidates[12–15]. Spiral generators, also called Vector Inversion Generators (VIGs), are small devices allowing to convert a DC input voltage u_0 into a short voltage pulse of amplitude much larger than u_0. These generators consist of a pair of conducting foils wound in a N-turn spiral of mean diameter D and a switch. The pair of conducting foils forms a capacitor that is charged initially at the DC input voltage u_0. The output pulse lasts a few tens of nanoseconds and is triggered by short-circuiting the capacitor by means of the switch causing a transient phenomenon to occur.

Fig. 1 illustrates the working principle of a spiral generator. Once the capacitor formed by the active and the passive conductors is fully charged at a voltage u_0, the electric fields of adjacent turns (schematically shown by the arrows in Fig. 1) cancel out, resulting in a zero net output voltage between the two ends of the active conductor. The outer extremity of the active waveguide is then short-circuited by the switch, causing an electromagnetic wave to propagate in the active waveguide, consisting of both conductors separated by the active dielectric. This wave reaches the extremity of the waveguide located at the inner part of the spiral (open circuit), which causes a reflection of the wave. When the reflected wave comes back at the outer extremity of the active waveguide, after a time T, all electric field directions are the same and the voltage is, in theory, multiplied by $2N$. After reflection of the wave on the impedance of the switch, the wave is reflected again and the output voltage goes back to 0 at $t = 2T$.

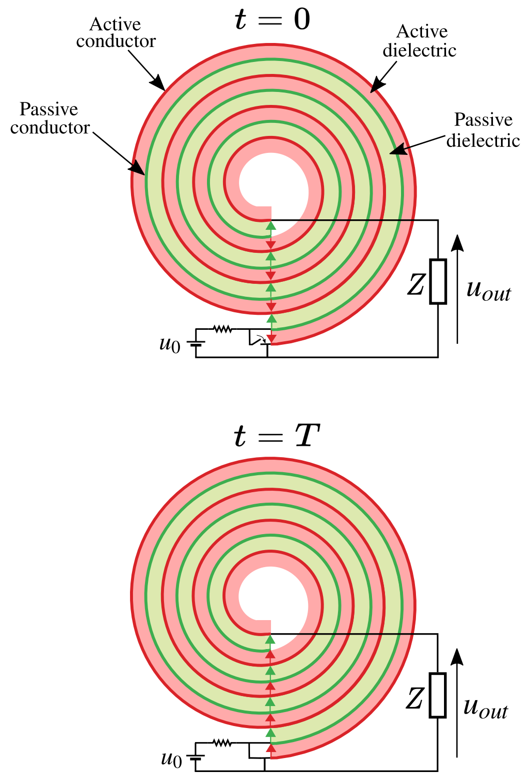

FIG. 1. Schematic diagram of the vector inversion phenomenon of a spiral generator.

Fig. 2 provides schematic time evolutions of the input and output voltages. The theoretical time evolution of the output voltage is a triangular waveform oscillating between 0 and $2Nu_0$ with a period $2T$. In practice however, the peak of the output voltage $u_{out}(t)$ is always below $2Nu_0$ because of imperfections in the vector inversion process. More precisely, the non zero inductance of the switch L_s causes the input voltage u_0 to reach zero in a time that is a non negligible fraction of T and the discharge of the passive waveguide (the one formed by both conductors separated by the passive dielectric) makes the process more complex than a simple vector addition with half of the vectors (the ones in the passive waveguide) remaining unchanged. The actual output voltage waveforms exhibits an oscillatory behavior and the second peak can sometimes exhibit higher voltages than the first peak in absolute value[16]. For this reason, two multiplication efficiencies are introduced: β_+ which is defined such that the amplitude of the first peak of $u_{out}(t)$ is equal to $2N(\beta_+)u_0$ and β_- which is defined such that the amplitude of the second peak of $u_{out}(t)$ is equal to $-2N(\beta_-)u_0$.

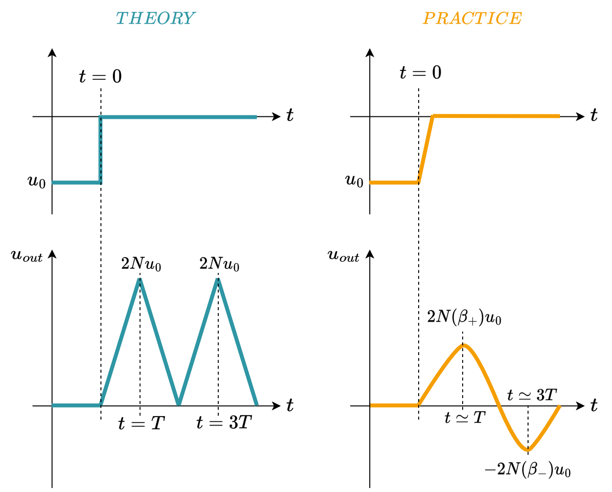

FIG. 2. Comparison of the input and output voltage waveforms of a vector inversion generator : theoretical waveforms of an ideal generator and typical experimental waveforms.

Spiral generators were first introduced by Fitch and Howell[12,13] in 1964. The authors explain the working principle of such generators but only provide a few approximated equations allowing one to predict the time evolution of the output voltage. In 1980, Rühl and Herziger[17] were the first to propose a transfer function linking u_{out} to u_0 in the Laplace domain. This model was later corrected by Bichenkov *et al.*[18] in 2007 and further developed by Pal'chikov *et al.*[19] in 2012. None of these transfer functions include resistive losses. The latter were mentioned by Fitch and Howell, who multiply the output voltage by a corrective factor and also recently by Yan *et al.*[16] in 2021 who introduce a global resistance of the spiral. In the present work, we use the works of Rühl, Herziger and Bichenkov as a starting point for an improved model that allows more precise predictions of the output voltage.

Our model considers new boundary conditions at the location of the switch and includes the local resistive losses in the form of a resistance per unit length of the waveguides. Contrary to the models proposed by Yan *et al.* and Pal'chikov *et al.*, we wish to obtain directly the analytical expression of the transfer function in the Laplace domain rather than a set of ordinary differential equations that are solved with a numerical scheme.

We then use our new transfer function to predict the values of the multiplication efficiencies from the knowledge of a set of dimensionless parameters involving the electrical and geometric characteristics of the spiral generator. The model described in this paper is also used to determine under which conditions a VIG provides a second voltage peak with a better multiplication efficiency than the first one, *i.e.* under which conditions $\beta_- > \beta_+$.

II. THEORY

In this section we first provide a brief summary of the published mathematical models which constitute the basis of our work. Then we describe our model for the prediction of the dimensionless multiplication coefficient $\beta(t) = \frac{u_{out}(t)}{2Nu_0}$. For clarity purpose, the following explanations will only contain the main steps to obtain the dimensionless Laplace transform of the multiplication coefficient. Using numerical methods to approximate inverse Laplace transforms, one can then easily retrieve $\beta(t)$. In our case, we used the Stehfest numerical method[20], available in the `mpmath` *Python* library. The full mathematical developments can be found in the appendices of this work.

A number of quantities need to be defined before considering the equations. First, a set of electric elements will repeatedly appear throughout the development, they are listed and defined here below:

- C', L' and R' respectively denote the capacitance, inductance and resistance per unit length of the active and passive waveguides, both waveguides are assumed to be characterized by the same parameters. Note that adapting these quantities to account for different properties of the two lines would only require a few extra steps in the developments,
- $Z_0 = \sqrt{\frac{L'}{C'}}$ is the lossless characteristic impedance of the active and passive waveguides,
- $C = \frac{C'\pi D}{2N}$ is the equivalent capacitance of the VIG during discharge, *i.e.* the capacitance between the output terminals,
- $L = N^2 L_{turn}$ is the inductance of the spiral formed by the active conductor. L_{turn} is the inductance of a single turn of the spiral. This assumes that all successive turns of the spiral have a similar equivalent diameter. Typically, L is in the order of tens to hundreds of microhenrys and L_{turn} in the order of tens of nanohenrys.

Second, different currents will appear in the equations leading to the transfer functions, they are listed below and are illustrated schematically in Fig. 3:

- $i_a(x)$ and $i_p(x)$ are the waveguide currents flowing respectively in the active and in the passive waveguides. x refers to the curvilinear abscissa along the waveguides, with $x = 0$ corresponding to the location of the switch at the outer side of the spiral and $x = x_{max} = N\pi D$ the location of the load, at the inner extremity of the spiral.

- $j_a(x)$ and $j_p(x)$ are a set of so called "circulating" current per unit length, able to flow across layers. $j_a(x)dx$ is a circulating current reaching the location x of the active conductor and $j_p(x)dx$ the circulating current reaching location x of the passive conductor.

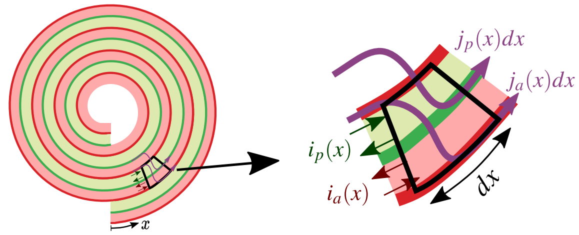

FIG. 3. Schematic representation of the currents appearing in a spiral generator. The currents are shown on a portion dx located at the curvilinear abscissa x of the spiral.

Finally, we define important dimensionless quantities which already appeared in some the published models[17,18]:

- $\omega_0 = \frac{T}{\sqrt{LC}}$: ratio of the back and forth travel time of the electromagnetic wave between both extremities of the active waveguide and the period of the oscillations of the equivalent LC circuit formed by the double spiral,

- $\tau_a = \frac{L_s}{Z_0 T}$: ratio of the "RL"-like time constant of the switch connected to the active waveguide and the back and forth travel time of the wave between both extremities of the active waveguide. "R" is here the characteristic impedance of the active waveguide and "L" is here the inductance of the switch L_s,

- $\tau_p = \frac{L_s + L_{outer}}{Z_0 T}$: ratio of the "RL"-like time constant of the switch in series with the outer turn of the active conductor connected to the passive waveguide and the back and forth travel time of the wave between both extremities of the active waveguide. "R" is here the characteristic impedance of the passive waveguide and "L" is here the inductance of the switch in series with the inductance of the outer turn of the active conductor L_{outer}. It is shown in Appendix B that τ_p is related to the previous two parameters by the relation: $\tau_p = \tau_a + \frac{4}{\omega_0^2}$,

- $\tau = \frac{T}{ZC}$: dimensionless parameter allowing to consider a load of Laplace impedance Z connected at the output of the generator. When no load is connected at the output terminals of the VIG, $\tau = 0$.

A. Understanding the model proposed by Rühl and Herziger

While Fitch and Howell[12] are the founders of spiral generators, Rühl and Herziger[17] were the first to propose a mathematical model allowing to predict the time evolution of the multiplication efficiency $\beta(t)$. Despite containing some typos and lacking explanations about how to obtain the equations presented in their mathematical development, the physical framework proposed in the article is eminently sensible. For this reason, the Rühl and Herziger model was chosen to be the starting point of the model we propose in our work. We review below the physics proposed in their paper. Appendix A contains the entire mathematical development.

The model proposed by Rühl and Herziger consists of a magnetic approach of the spiral generator. Their model is obtained by considering the active conductor as an inductor of N turns embracing the magnetic flux generated by all the currents flowing in loops inside the double spiral. Using Faraday's law of induction, the authors could link this magnetic flux to the output voltage of the generator. There are three contributions to this magnetic flux: $j_a(x)$ the leakage current per unit length flowing from one turn of the active conductor to an adjacent turn of the same conductor, $j_p(x)$ which corresponds to $j_a(x)$ for the passive conductor and i_z, the current flowing through the load Z connected between the ends of the active conductor.

Using the superposition theorem and the telegrapher's equations for the electromagnetic wave propagation in the waveguides, they were able to obtain a dimensionless transfer function $B_1(p)$ (Eq. A11) which we will refer to as Model 1 throughout the paper.

B. Limitation of the model proposed by Rühl and Herziger

A non-negligible approximation in the development of Rühl and Herziger lies in the boundary conditions. It is assumed in their model that there is no current flowing at any end of the passive waveguide, *i.e.* $I_p(x = 0, s) = I_p(x = x_{max}, s) = 0$. Within this assumption, there are no waveguide currents at any location of the passive waveguide, *i.e.* $I_p(x, s) = 0$ and the current flowing through the switch results from the waveguide currents flowing in the active waveguide only: $I_s = I_a(x = 0)$.

In reality, the terminology 'passive waveguide' is misleading since there are non-zero waveguide currents in this waveguide. The reason is the following: when the active line is short-circuited by the switch, the passive line gets short-circuited as well via the switch in series with the outer turn of the active conductor, as shown schematically in Fig. 4. This point was already noticed by Bichenkov *et al.*[18] in their mathematical developments. Using an electrostatic approach rather than a magnetic approach, Bichenkov *et al.* found a transfer function consistent with that of Rühl and Herziger but improved it with a set of boundary conditions that considers a wave propagating in the passive waveguide. This transfer function $B_2(p)$ (Eq. B15) will later be referred to as Model 2. In the limit $\tau_p \rightarrow +\infty$, *i.e.* when the passive waveguide as an infinite rise time, $B_2(p)$ becomes similar to $B_1(p)$ and one recovers Model 1.

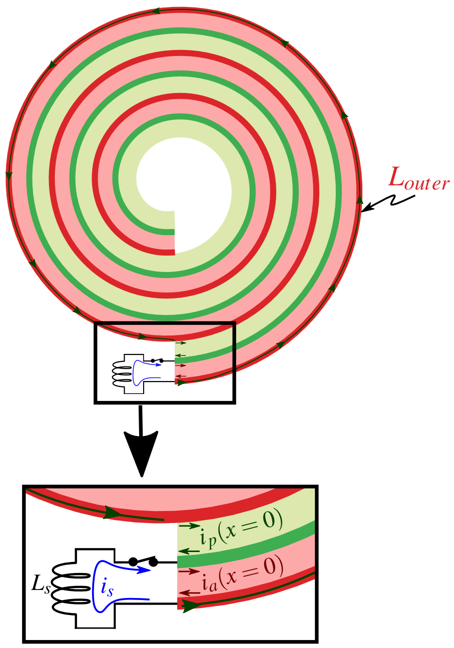

FIG. 4. Schematic representation of the currents appearing in the switch, according to Kirchhoff's current law.

C. Extension of the model

In the present work, we propose an improved version of the models mentioned above. The improvement lies in two points regarding (i) the current in the switch and (ii) the losses of the conductor.

1. *Boundary conditions at the location of the switch*

We first consider the current in the switch. Even if Bichenkov *et al.* considered a wave propagating in the passive line, the interactions between I_a and I_p in the switch were neglected. This approximation is valid when $\zeta = \frac{\tau_a}{\tau_p} << 1$, *i.e.* when the passive line is much slower than the active line, but introduces an error when the switch exhibits imperfections. We determine here below the transfer function $B_3(p)$ taking into account the interaction between both waveguide currents. We follow an approach similar to that followed by Rühl and Herziger but we consider a wave propagating in the passive line and with the complete expression of the switch current $I_s(s)$ obtained with Kirchhoff's current law at the location of the switch, as illustrated in Fig. 4.

As for the previous models, the entire mathematical development are given in Appendix B. The updated Laplace equation of the output voltage U_{out} is:

$$U_{out}(s) = \frac{-s\left[I_a(x=0,s)+I_p(x=0,s)\right]}{2NC(s^2+\frac{1}{ZC}s+\frac{1}{LC})}, \tag{1}$$

where the currents appearing in the numerator are obtained using the following boundary conditions:

$$\left\{\begin{array}{rcl} U_a(x=0,s) &=& \frac{u_0}{s} - sL_sI_s(s), \\ U_p(x=0,s) &=& \frac{-u_0}{s} - sL_sI_s(s) - sL_{outer}I_p(x=0,s), \\ I_s(s) &=& I_a(x=0,s) - I_p(x=0,s). \end{array}\right. \tag{2}$$

The main differences with respect to the Bichenkov can be seen in the above equations: at the start of the waveguides ($x=0$) the voltage U_a across the active waveguide also depends on the current in the passive waveguide (I_p, through the current in the switch I_s), and the voltage U_p across the passive waveguide also depends on the current in the active waveguide (I_a, through the current in the switch I_s). This interaction between the electric parameters of the two waveguides was neglected in the approaches used up to now. Remarkably, it yields the following dimensionless transfer function that can be calculated analytically, at the expense of heavier developments that are described in Appendix B:

$$B_3(p) = \frac{-pF(p)}{p^2+(1-G(p))\left(\tau p+\omega_0^2\right)}, \tag{3}$$

with:

$$F(p) = \frac{A(p)-P(p)}{1-p^4\tau_a^2A(p)P(p)}, \tag{4}$$

$$G(p) = \frac{A(p)+P(p)+2p^2\tau_aA(p)P(p)}{1-p^4\tau_a^2A(p)P(p)}, \tag{5}$$

$$A(p) = \left[p\coth\left(\frac{p}{2}\right)+p^2\tau_a\right]^{-1}, \tag{6}$$

$$P(p) = \left[p\coth\left(\frac{p}{2}\right)+p^2\tau_p\right]^{-1}. \tag{7}$$

Considering the above equations with the limit $\tau_a \rightarrow 0$ (when the switch exhibits and ideal behavior), one obtains $F(p) = A(p) - P(p)$ and $G(p) = A(p) + P(p)$, which corresponds to the transfer function of Model 2.

2. *Resistive losses*

Next we consider the losses. Another common assumption in the published models is to neglect resistive losses in the conductors as well as in the switch. Our model is suited to take easily both resistive losses (conductor of the spiral and switch) into account in the equations describing the physics of the generator. In view of maximizing the amplitude of the peaks of the output voltage $u_{out}(t)$, it is important to optimize β_+ and β_- but also to increase the number of turns as $u_{out}(t) \propto 2N\beta(t)$. Yet, as the number of turns increases, the waveguides are longer and the damping of the waves while travelling the waveguides also increases, causing $\beta(t)$ to decrease in absolute value. Therefore, the impact of the losses on the output voltage becomes particularly relevant when the number of turns increases.

When considering the losses, a question arises related to the value of R', the resistance per unit length of the conductors in the active and passive waveguides. To consider the skin depth δ over which the current flows inside the conductors, one must define an equivalent working frequency of the spiral generators. The oscillations of the transient time evolution of the output voltage being close to $4T$ (*cf.* schematic waveforms shown in Fig. 2), one can define an approximated equivalent frequency $f_{eq} = \frac{1}{4T}$. This frequency makes it possible to estimate $\delta = (\sigma\pi f_{eq}\mu)^{-\frac{1}{2}}$, with μ the magnetic permeability of the waveguides and σ the conductivity of the conductors. One can derive the losses per unit length in the conductors: $R' = 2(\sigma\delta w)^{-1}$ if the skin depth is smaller than the thickness of the conductor t_{cond} or $R' = 2(\sigma t_{cond} w)^{-1}$ otherwise, where w is the height of the conductors. The factor 2 comes from the fact that the waveguides consists of 2 conductors.

One can then update the telegrapher's equations to account for R' and update the boundary conditions at $x = 0$ by replacing sL_s by $Z_s = sL_s + R_s$ and sL_{outer} by $Z_{outer} = sL_{outer} + \frac{1}{2}R'\pi D_{outer}$, with D_{outer} the outer diameter of the active conductor and the $\frac{1}{2}$ factor coming from the fact that the outer turn consists of only one conductor. It is then possible to obtain an updated dimensionless transfer function $B(p)$ of the multiplication coefficient. The entire development is provided in Appendix B. At certain stages of the mathematical development, the following dimensionless parameters appear:

- $\rho_0 = \frac{R'T}{L'}$: the dimensionless quality factor of the conductors,
- $\rho_a = \frac{R_s}{\sqrt{\frac{L'}{C'}}}$: the ratio of the resistance of the switch and the lossless characteristic impedance of the waveguides,
- $\rho_p = \frac{R_s+R_{outer}}{\sqrt{\frac{L'}{C'}}}$: the ratio of the resistance of the switch in series with the outer turn of the active conductor and the lossless characteristic impedance of the waveguides.

Note that ρ_a and ρ_p are small quantities that can usually be neglected, which is not true for ρ_0 as will be shown later in the article.

Taking the losses into account yields the following updated transfer function $B(p)$:

$$\tilde{B}_3(p) = \frac{-p\tilde{F}(p)}{p^2 + \left(1-\tilde{G}(p)\right)\left(\tau p + \omega_0^2\right)}, \tag{8}$$

with the tilde values being updates of the previous quantities with additional terms accounting for resistive losses:

$$\tilde{F}(p) = \frac{\tilde{A}(p) - \tilde{P}(p)}{1-\left(p^4\tau_a^2 + 2p^3\tau_a\rho_a + p^2\rho_a\right)\tilde{A}(p)\tilde{P}(p)}, \tag{9}$$

$$\tilde{G}(p) = \frac{\tilde{A}(p) + \tilde{P}(p) + 2\left(p^2\tau_a + p\rho_a\right)\tilde{A}(p)\tilde{P}(p)}{1-\left(p^4\tau_a^2 + 2p^3\tau_a\rho_a + p^2\rho_a\right)\tilde{A}(p)\tilde{P}(p)}, \tag{10}$$

$$\tilde{A}(p) = \left[p\sqrt{1+\frac{\rho_0}{p}}\coth\left(\frac{p}{2}\sqrt{1+\frac{\rho_0}{p}}\right) + p^2\tau_a + p\rho_a\right]^{-1}, \tag{11}$$

$$\tilde{P}(p) = \left[p\sqrt{1+\frac{\rho_0}{p}}\coth\left(\frac{p}{2}\sqrt{1+\frac{\rho_0}{p}}\right) + p^2\tau_p + p\rho_p\right]^{-1}. \tag{12}$$

This final model will be called Model 3 throughout the rest of the article. In can be readily seen that in the limit $\tau_a \to 0$, $\rho_a \to 0$, $\rho_p \to 0$ and $\rho_0 \to 0$, one recovers the transfer function of Model 2. Although these final relations appear very complicated, it will be shown in the results that these additional terms reflect some real practical phenomena and allow to obtain a better agreement with experimental measurements.

D. Switch current

As $I_a(x=0,s)$ and $I_p(x=0,s)$ are quantities that appear naturally in the mathematical developments leading to the transfer functions of the output voltage and as $I_s = I_a(x = 0,s) - I_p(x = 0,s)$, it is possible to obtain directly the analytical expression of the switch current in the Laplace domain with a few extra lines of algebra. Appendix C contains the mathematical developments as well as the final expressions of the switch current and of the contribution of each waveguide current to the current in the switch.

III. EXPERIMENT

In order to validate the proposed model and compare it to other published models, we measured the time evolution of the output voltage of the spiral generator shown in Fig. 5. Between the copper foils used as conductors, a single sheet of Kapton™ is used as dielectric layer. The characteristics of this generator are provided in Table I.

TABLE I. Characteristics of the vector inversion generator used during the experimental measurements.

Characteristic	Symbol	Value
Number of turns	N	40
Mean diameter	D	70 mm
Height	w	25.4 mm
Conductor thickness	t_{cond}	40 μm
Dielectric thickness	t_{diel}	50 μm
Relative permittivity	ε_r	3.4

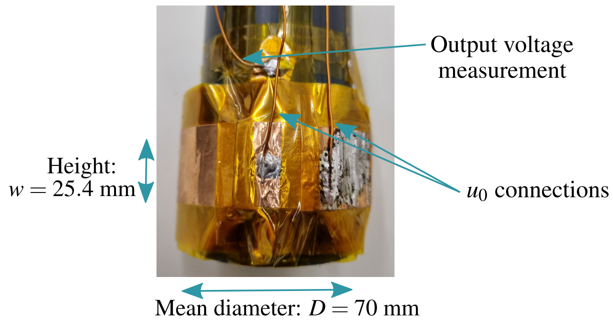

FIG. 5. Picture of the vector inversion generator used during the experimental measurements.

A way to assess the influence of the losses of the conductors on the output voltage while keeping other parameters almost unchanged, is to carry a similar set of experiments at a different temperature. It was therefore decided to perform the experiments at room temperature (300 K) and in a liquid nitrogen reservoir (77 K). As the coefficient of thermal expansion of copper is about 16.4 μm/(m K) and the coefficient of thermal expansion of the Kapton™ sheet we used is 20 μm/(m K), it corresponds to a change in thickness of 0.15 μm for the copper film and 0.23 μm for the Kapton™ film. This validates the hypothesis that the geometric parameters are almost unchanged when cooling down to cryogenic temperatures[21,22]. For safety reasons in the cryogenic set-up, all experiments were performed with a low input voltage of -10 V. As the output voltage never exceeded 350 V, the waveforms were measured with a 10:1 voltage probe of capacitance $C_{probe} = 16$ pF. This capacitance was considered in the models by assigning $\tau = \frac{T}{ZC} = p\frac{C_{probe}}{C}$. In order to not place the voltage probe inside the liquid nitrogen reservoir, the voltage measurement was shifted about 70 mm away away from the extremities of the spiral generator. It was verified experimentally that these extra wires connected at the extremity of the spiral generator have no significant effect on the measured data (i.e. <2% relative difference for the amplitude of the first peak of $u_{out}(t)$ and <3.5% relative difference for the amplitude of the second peak). We also used our analytical model to assess the influence of the wire length on $u_{out}(t)$ (by changing the expression of the dimensionless parameter τ to consider a LC-series load) and it showed no difference at all in the predicted output voltage curves caused by the inductance of 70-mm-long wires.

In order to investigate the effect of τ_a on $\beta(t)$ predicted by each model, three bespoke, low voltage mechanical switches with different inductances L_s were created. The first switch (hereafter called 'SW-A') consists of a 1.5 mm diameter Cu-wire (3 mm with the sheath). One extremity of this wire was soldered to the active conductor of the spiral generator while the other side of this wire was brought mechanically in contact of the passive conductor by means of a small PTFE rod. The resulting switch inductance is approximated to that of a single circular loop[23] with a diameter of 15 mm, resulting to an estimated switch inductance L_s of 25 nH. In order to artificially increase the value of the inductance of the switch, two other switches were created by placing an additional coil of diameter 15 mm in series with the wire. The second switch (hereafter called 'SW-B') was created by placing a single-turn coil in series with the wire and the third switch (hereafter called 'SW-C') with a three-turn coil. Using Rayleigh and Niven's formula[24], SW-B has an estimated inductance of 55 nH and SW-C an estimated inductance of 165 nH. The resulting experimental setup is shown in Fig. 6.

TABLE II. Summary of the dimensionless parameters corresponding to the VIG configurations that were tested experimentally.

Parameter	Switch SW-A	Switch SW-B	Switch SW-C
τ_a	0.55	1.21	3.62
ω_0	1.41	1.41	1.41
τ_p	2.55	3.21	5.63
$\zeta = \frac{\tau_a}{\tau_p}$	0.22	0.38	0.64
ρ_0 (300 K - 77 K)	1.51 - 0.47	1.51 - 0.47	1.51 - 0.47
ρ_a, ρ_p	$\simeq 0$	$\simeq 0$	$\simeq 0$

The behavior of the spiral generator was measured at room temperature or when immersed in liquid nitrogen, with the three switches mentioned before. The change in conductivity σ_{Cu} of the copper conductors before and after being immersed in the liquid nitrogen was measured experimentally beforehand by means of a Four-Wire Kelvin measurement. At room temperature, $\sigma_{Cu} = 5.96 \cdot 10^7$ S/m leading to a estimated skin depth $\delta = 44\,\mu$m which is larger than the thickness of the conductive foil. At cryogenic temperature, we measured that the conductivity was increased by a factor 8.5. The new estimated skin depth is about 15 μm meaning that this time, the skin effect does affect the resistance of the conductors of the spiral generator. Therefore, one should note that the ratio of the loss parameters before and after being cooled down to 77 K is not proportional to the ratio of the conductivities as the skin effect limits the resistance only in one case.

With the experimental setup presented in the previous section, it was possible to test our spiral generator with three different values of τ_a ($\tau_a = 0.55, \tau_a = 1.21$ and $\tau_a = 3.62$) and two values of ρ_0 ($\rho_0 = 1.51$ and $\rho_0 = 0.47$). Table II provides a summary of all the dimensionless parameters corresponding to the configurations that we tested experimentally.

IV. RESULTS

A. Validation of the proposed model

In order to validate the model we propose in this work, we compared the predictions of $\beta(t) = \frac{u_{out}(t)}{2Nu_0}$ provided by the three models to experimental measurements. Let us recall here that due to their value in the range 25-165 nH, the switch inductances L_s could not be measured precisely

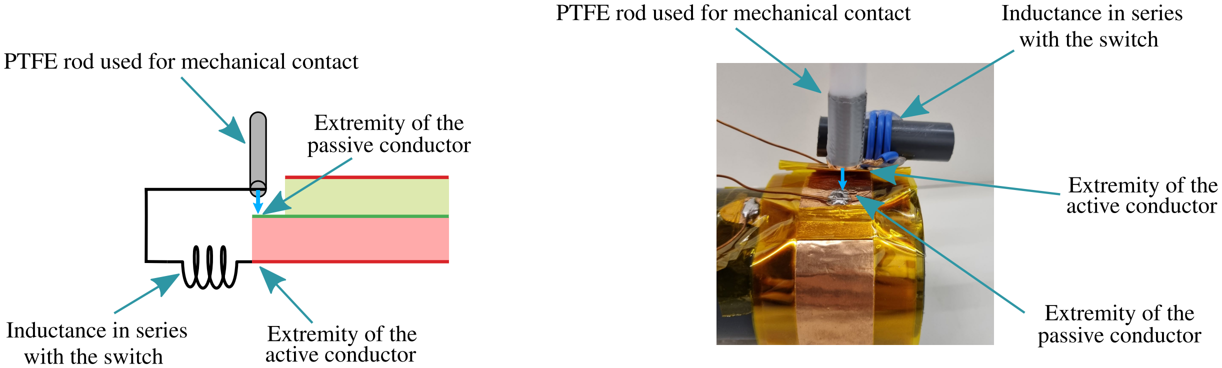

FIG. 6. Picture of the experimental setup used to measure the time evolution of the output voltage. The PTFE rod is used to bring the second extremity of the coil in contact with the passive conductor, shorting the input of the generator with an inductance given by the blue coil.

but rather estimated using formulas from the literature, as described in Sect. III. The resulting L_s values are therefore predicted within a given uncertainty of $\sim 10\%$. As a result, it is of interest to compute the predictions of the models by changing L_s in a range of 10% around the estimated values. The results are shown in Fig. 7, comparing the β_+ and β_- values provided by each model in the range $[0.9L_s; 1.1L_s]$ to the β_+ and β_- values obtained experimentally. Additionally, Fig. 8 shows the comparison between models and experimental measurements of the time evolution of $\beta(t)$ for the three values of L_s, at both room temperature and cryogenic temperatures. One can directly observe in Figures 7 and 8 that the predictions provided by Model 1 and Model 2 (green and blue curves) are the same for room temperature and cryogenic temperature as the only parameters that changes is ρ_0, the parameter that asses the losses, which only appears in Model 3. Table III contains quantitative data about the different experimental scenarios. More precisely, it contains the relative differences between the predictions of the models and the experimental measurements at room temperature and at cryogenic temperature. These differences were computed for the amplitudes of β_+ and β_- but also for the time at which these values are observed.

TABLE III. Relative difference of the multiplication efficiencies β_+ and β_- as well as the timing at which they occur between experimental measurements and predictions of the model at cryogenic temperature. Values are computed as follows: $\frac{model-experimental}{experimental}$. The first value corresponds to the amplitude of β and the value between parentheses corresponds to the timing.

		Model 1	Model 2	Model 3
Room temperature				
β_+	SW-A	115% (10%)	34% (1%)	13% (-7%)
	SW-B	92% (20%)	-5% (7%)	-5% (-2%)
	SW-C	92% (30%)	-42% (20%)	-15% (-1%)
β_-	SW-A	66% (11%)	46% (1%)	-4% (-1%)
	SW-B	126% (14%)	53% (7%)	3% (-5%)
	SW-C	150% (24%)	11% (20%)	-11% (-4%)
Cryogenic temperature		Model 1	Model 2	Model 3
β_+	SW-A	59% (18%)	0% (8%)	0% (6%)
	SW-B	73% (20%)	-14% (7%)	0% (0%)
	SW-C	74% (41%)	-47% (30%)	-9% (4%)
β_-	SW-A	50% (15%)	32% (7%)	8% (6%)
	SW-B	73% (17%)	17% (7%)	-5% (-1%)
	SW-C	87% (29%)	-16% (21%)	-33% (-2%)

We first consider the experimental data obtained with SW-A. One can notice that, for the first peak, Model 2 and Model 3 are in close agreement with experimental data, both for timing and amplitude. Model 1, on the contrary, predicts values of β_+ that are much larger than the experimental measurements. Quantitatively, Model 1 overestimates β_+ by more than 100%. Regarding the second peak, the first negative one, the predictions of Model 1 are again much larger than the experimental measurements, which validates the negative impact of the discharge of the passive waveguide on the output voltage generated by spiral generators. Model 2 begins to diverge from the experimental measurements, which is not the case for Model 3. The difference between the measurements of β_- and the values of β_- predicted by Model 2 are different at room temperature and at cryogenic temperature. This emphasizes the importance of considering resistive losses when modelling spiral generators, as they cause damping over time. Quantitatively, with SW-A, the experimental measurement of β_+ goes from 0.25 to 0.31 and the experimental measurement of β_- goes from 0.44 to 0.50 when ρ_0 is reduced from 1.51 (at 300K) to 0.47 (at 77K). This result shows that resistive losses have a non-negligible impact on the multiplication efficiencies and cannot be neglected.

As far as SW-B is concerned, similar conclusions can be taken as with SW-A: Model 1 overestimates β_+ and β_-, Model 2 provides a good estimations of β_+ but overestimates β_- and Model 3 is in close agreement with the experimental data for both peaks of $\beta(t)$. The main difference between both experiments is that the additional coil in series with the switch causes a decreases in the absolute value of $\beta(t)$.

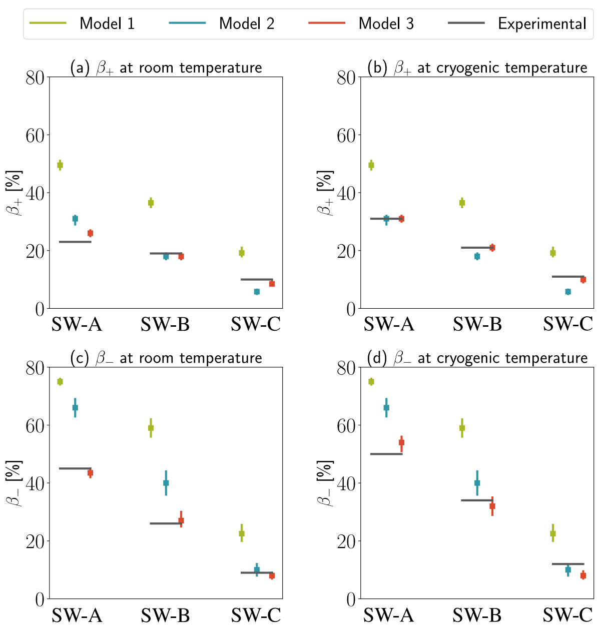

FIG. 7. Summary of all the β_+ and β_- values for all the configurations that were tested experimentally. As L_s was estimated with a given uncertainty, the values provided by each model are computed with each model in an interval $L_s \pm 0.1 L_s$.

When looking at the waveforms obtained with SW-C, one can first see that the experimental values of β_+ and β_- are lower compared to those obtained with SW-B. Quantitatively, between SW-A and SW-C, the experimental values of β_+ went from 23% to 10% and the experimental values of β_- from 45% to 9%. This result confirms the well-established fact[25] that τ_a should be as low as possible to increase the multiplication efficiencies, *i.e.* that the inductance of the switch should be as low as possible. As before, the curves obtained with Model 3 provide better estimations of $\beta(t)$ than the curves obtained with Model 1 and Model 2. The error on β_+ and β_- introduced by Model 2 is smaller with SW-C, but one can observe that the blue curves are now time shifted compared to the experimental waveforms. The predicted peaks of $u_{out}(t)$ given by Model 2 take place slower than what is observed experimentally. In fact, the relative time difference between the experimental peaks and the predictions of the Model 2 can go up to 30%. This shows that neglecting the interaction between i_a and i_p in the switch has indeed an influence on $\beta(t)$, not only on the amplitude but also on the timings. This time delay appearing when τ_a increases is consistent with the mathematical models, as it was observed that, when neglecting losses, Model 2 and Model 3 are similar when $\tau_a \to 0$, when the switch is ideal. This observation also confirms the statement of Bichenkov *et al*[18] stating that the interaction of waveguide currents is negligible when $\tau_a \ll \tau_p \Leftrightarrow \zeta \ll 1$, meaning that either the switch is ideal or the inductance of the outer turn of the spiral generator L_{outer} is much larger than the inductance of the switch L_s. As a matter of fact, this time shift between experimental data and Model 2 appears for $\zeta = 0.64$ (SW-C) but was almost insignificant for $\zeta = 0.22$ (SW-A) and $\zeta = 0.38$ (SW-B).

Even though the model described in this work (Model 3) fits the experimental curves closely for the two first peaks of $u_{out}(t)$, it does not perfectly match the time evolution of the experimental results over a longer period of time. This can be observed in Fig. 9 showing the time evolution of $\beta(t)$ with SW-B at room temperature, but over a time window of about 2.5 μs (against 0.7 μs in Fig. 8). One can see that the $\beta(t)$ curve predicted by Model 3 shows a similar oscillatory behavior as the experimental curve, but the period of these oscillations is higher on the prediction of Model 3 than in the experimental curve. One plausible explanation lies in the way the skin depth δ is computed in our model. δ is obtained by computing an equivalent frequency $f_{eq} = \frac{1}{4T}$ which is an approximation as the waveforms is not a perfect sine and as the period of the oscillations is not exactly equal to $4T$.

B. Deeper comparison between Model 2 and Model 3

1. *Switch current*

To obtain a deeper comparison between our updated model (Model 3) and the model proposed by Bichenkov *et al.* (Model 2) that does not consider losses nor current interaction near the switch, we can first compare what happens at the location of the switch. Model 1 is not considered anymore at this stage of the article as the experimental results showed that the assumptions that lead to Model 1 caused a too significant difference between predictions and experimental measurements. Fig. 10 shows curves of $i_a(x=0,t)$, $i_p(x=0,t)$ and $i_s(t) = i_a(x=0,t) - i_p(x=0,t)$, predicted with Model 2, Model 3 with $\rho_0 = 0$ (to only investigate the effect of our new boundary conditions) and Model 3 with $\rho_0 \neq 0$ (to also investigate the fact that we consider resistive losses). Note that for the computation of the switch current shown in Fig. 10, we do not consider the presence of a voltage probe ($\tau = 0$). The figure also contains $u_{out}(t)$ prediction waveforms given by Model 3. Model 3 was chosen rather than experimental measurements for the $u_{out}(t)$ curves since the condition $\tau = 0$ can be inserted readily in the model. This is in contrast with experimental measurements for which the delay caused by the finite capacitance of the probe always affects the voltage curves.

Figures 10a to 10d show the curves for SW-A (corresponding to the smallest switch inductance tested experimentally). It can first be seen that the behavior of the switch current over time shows similar oscillations with each model. The main difference being that the envelopes of the curves decrease a first time when considering current interaction near the switch and further decrease because of damping when ρ_0 is considered non zero. This means that Model 2, in addition to overestimating the output voltage, also overestimates the current in the switch. One can also notice the presence of a small difference in the period of the oscillations of the curves obtained with Model 2 and the curves obtained with Model 3

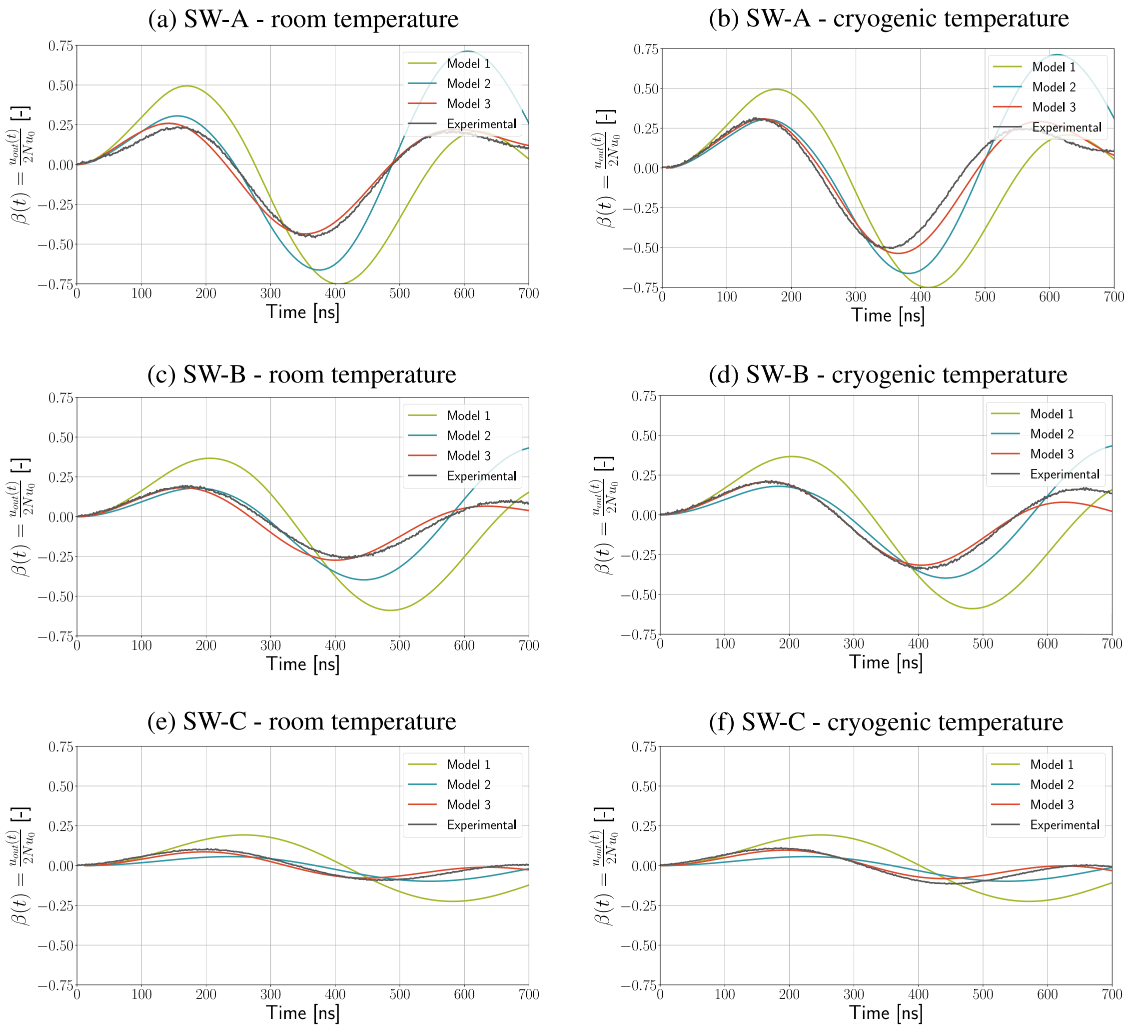

FIG. 8. Comparison of the time evolution of the voltage multiplication efficiency $\beta(t)$ measured experimentally and predicted by the models for different values of inductances placed in series with the mechanical switch and at different temperatures.

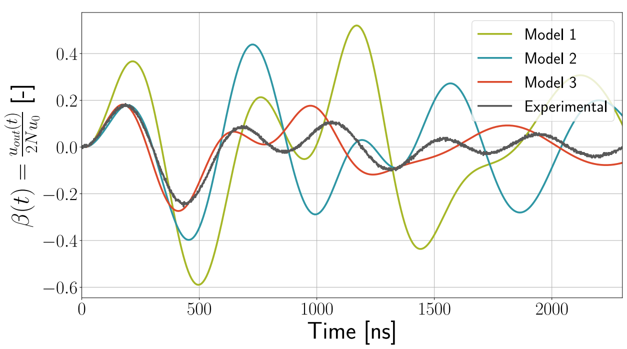

FIG. 9. Evolution of $\beta(t)$ with switch SW-B at room temperature for a long period of time.

(with or without considering losses). On the contrary, the period of the oscillations predicted by Model 3 without losses and Model 3 with losses are almost the same.

Figures 10e to 10h show a similar set of curves for SW-C (*i.e.* the largest switch inductance tested experimentally). One can see in Figure10g that the switch current $i_s(t)$ predicted by Model 2 and the associated contribution of the active waveguide $i_a(x=0,t)$, shown in Fig. 10e, have a period of oscillations that exceeds the time window of the graph. On the contrary, when looking at the same curves but predicted by Model 3, one can see more than an entire oscillation of $i_a(x=0,t)$ over the considered time window. This shows that for higher values of L_s, the estimated switch currents obtained with Model 2 and Model 3 show a major qualitative difference in addition to the difference in amplitude.

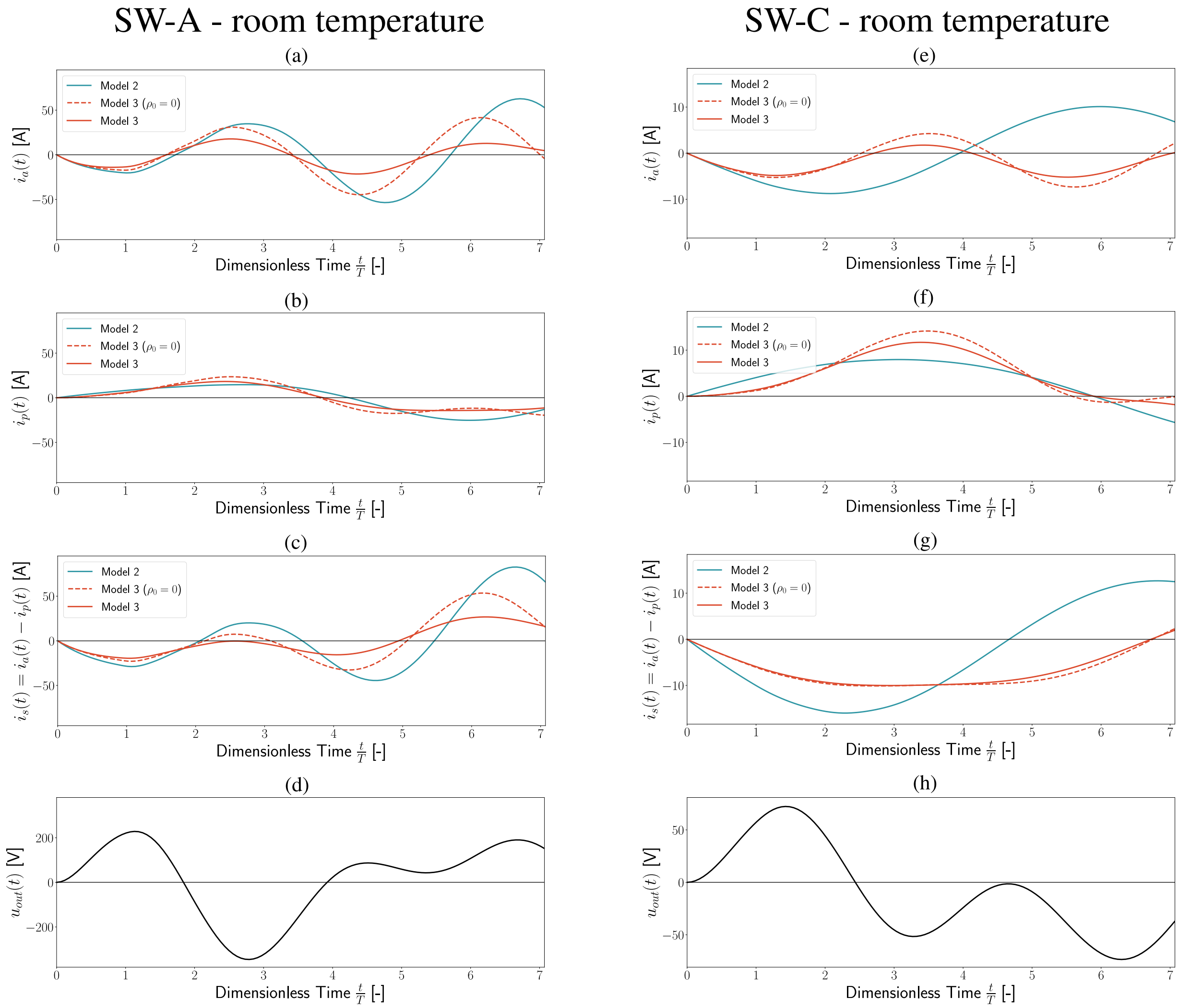

FIG. 10. Comparison of the switch current $i_s(t)$ (and its two contributions from the active and passive waveguides) obtained with Model 2 and Model 3 (with and without losses) compared to the predicted output voltage given by Model 3. The curves are obtained considering that there is no load connected at the output of the spiral generator ($\tau = 0$). (a) $i_a(t)$ with switch SW-A, (b) $i_p(t)$ with switch SW-A, (c) $i_s(t)$ with switch SW-A, (d) predicted $u_{out}(t)$ with switch SW-A, (e) $i_a(t)$ with switch SW-C, (f) $i_p(t)$ with switch SW-C, (g) $i_s(t)$ with switch SW-C, (h) predicted $u_{out}(t)$ with switch SW-C.

Fig. 10 allows to provide some explanations to the output voltages plotted in Fig. 8. We first saw that the main difference in the $\beta(t)$ predictions between Model 2 and Model 3 when ζ increases (when the inductance L_{outer} decreases for a fixed value of L_s) is a time shift in the $u_{out}(t)$ curves. This might come from the fact that when neglecting the interactions between the currents inside the switch, the dynamics of $i_a(t)$ become slower. Everything happens thus as if the switch had a higher inductance. This virtual increase in L_s could be the reason why the blue $\beta(t)$ curves (Model 2) in Fig. 8e and 8g show some delay compared to the experimental measurements and no longer predict higher β_+ and β_- values than the red curves (Model 3). Fig. 10 makes it also possible to validate the fact that the differences in the predictions of the values of β_+ and β_- come from the damping caused by resistive losses which is not considered in Model 2.

2. Maps of β_+ and β_- as a function of the dimensionless parameters

To further deepen the comparison between Model 2 and Model 3, we also computed the value of β_+ and β_- for values of τ_a and ω_0 ranging from 0.1 to 3. Values lower than 0.1 were not computed to avoid divisions by zero. This is not a problem as it is unlikely to reach such low values with experimental configurations anyway. Similarly, values above 3 were not computed as the corresponding multiplication efficiencies are not high enough for an acceptable multiplication efficiency (as observed with the experimental data obtained with SW-C). Such ($\omega_0 - \tau_a$) maps of β_+ and β_- were computed for Model 2 and for Model 3 with different loss parameters $\rho_0 = 0$, $\rho_0 = 0.5$, $\rho_0 = 1$, $\rho_0 = 1.5$ and $\rho_0 = 2$ (parameters affecting this loss parameters mainly are the length of the spiral, dictated by the number of turns N and the mean diameter D as well as the conductivity of the conductor material). The results are shown in Figures 11 for β_+ and in Fig. 12 for β_-. These two figures also contain several dots which are the estimated values of β_+ and β_- predicted by the models for configurations of VIGs presented in the literature[18,19,26,27]. The maps also contain stars representing the estimated values of β_+ and β_- predicted by the models for the configurations tested in our lab to validate our model. In addition, the figure contains isocurves of $\zeta = \frac{\tau_a}{\tau_p} = \frac{L_s}{L_{outer}+L_s}$ giving some information about the value of τ_p.

A general observation one can make in these two figures is that, both for β_+ and β_-, the maps gets closer to cold colors as ρ_0 increases, meaning that both multiplication efficiencies decrease as ρ_0 increases. This validates the importance of considering the losses in a mathematical model and the negative influence of the damping of the wave on the multiplication process.

($\omega_0 - \tau_a$) maps of β_+

First, we discuss the ($\omega_0 - \tau_a$) map of β_+ shown in Fig. 11. To only compare the influence of the different boundary conditions that were used to obtain the models, one should compare the map obtained using Model 2 and Model 3 with $\rho_0 = 0$. There is almost no difference between the predictions provided by the models; the only noticeable difference is that Model 3 provides estimated values of β_+ that are slightly smaller than those given by Model 2 in the right part of the maps, *i.e.* for large values of τ_a. Again, this makes sense as both models are the same when $\tau_a \to 0$. One can also see that all the maps related to β_+ show that for a given value of τ_a, ζ should be as low as possible to increase β_+. This observation validates the fact that the discharge of the passive waveguide decreases the multiplication efficiency and therefore that τ_p should be maximised to delay the discharge of the passive waveguide by having an inductance L_{outer} such that $L_{outer} + L_s >> L_{outer}$. The later can practically be obtained by increasing the mean diameter of the spiral or by adding a magnetic material.

When there are no losses, the maps obtained with both models predict that β_+ is maximised in the lower left corner of the map. This means that τ_a should be minimised as well, so that the input voltage reaches 0 volts much faster than the back and forth travel time of the wave. When $\rho_0 \neq 0$, Model 3 predicts a different behavior: ω_0 should still be as low as possible for a given τ_a, but τ_a must not necessary be minimised to maximise β_+. More precisely, below $\omega_0 \simeq 1$, some regions appear where increasing τ_a can lead to larger values of β_+ for a given value of ω_0. This can probably be explained by the presence of a trade-off between the damping of the waves during their travel time and the decrease of β_+ caused by the time required to have the input voltage reaching 0 volts. Even though these observations are of interest to understand the physics of spiral generators, one can also observe that all the dots and stars representing actual VIG configurations investigated experimentally are characterised by ω_0 values above = 1, meaning that for these configurations, τ_a should in fact be minimised.

($\omega_0 - \tau_a$) maps of β_-

Second, we can compare the ($\omega_0 - \tau_a$) maps of Fig. 12 of the predictions of β_-. This time, the difference between both models is already noticeable for τ_a = 0.1. The estimated value of β_- obtained with Model 2 are higher in the entire map, as evidenced by a warmer set of colors in the entire ($\omega_0 - \tau_a$) plane. One can also notice that the maps of β_- are split in three regions. On the bottom left region of these maps, β_- is close to zero. This region corresponds to the locations where β_+ is maximised and defines the set of parameters where the VIG almost works in the optimal conditions, *i.e.* when the output waveforms resembles the schematic ones shown in Fig. 2. This means that the output voltage waveform $u_{out}(t)$ is almost triangular, *i.e.* with small values of β_-. Then, as ζ increases, the output voltage is no longer triangular and β_- increases as the second peak of $u_{out}(t)$ is no longer close to zero. Finally, as ω_0 and τ_a further increase, we reach the top right corner where the VIG produces low multiplication efficiencies, as was observed for β_+.

Still about the β_- maps, one can see that starting from $\rho_0 = 1$, $\beta_- > 0$ in the lower left corner of the maps. One only reaches $\beta_- = 0$ near $\omega_0 \simeq \tau_a \simeq 0.3$. This lower left corner can actually be split into three regions, those regions are illustrated in the map $\rho_0 = 1$. In region (i), the first minimum of $u_{out}(t)$ is actually positive, meaning that β_- is negative. The amplitude of the first minimum of $u_{out}(t)$ gets closer and closer to zero until reaching zero in region (ii). Then, as ζ keeps increasing, we enter region (iii) where β_- becomes positive, meaning that the second peak of $u_{out}(t)$ is indeed negative. This means that the strange color behavior near the $\omega_0 = \tau_a = 0.1$ corner of the maps is actually due to the fact that we plot the absolute values of β_- while in reality, β_- changes signs in the region where the output voltage is almost triangular.

Finally, there is one last odd behavior in the map with $\rho_0 = 2$, corresponding the red dashed ellipse near $\omega_0 = 0.5$ and $\tau_a = 0.1$. β_- suddenly reaches values much higher than in the neighboring zone of the map, causing a discontinuity in the map. When looking at predicted $u_{out}(t)$ curves in that region, the second and third peak of $u_{out}(t)$ actually merge, causing the output voltage to remain almost constant with a slightly negative slope rather than reaching a minimum. This causes our algorithm to return the value of the next negative peak of $u_{out}(t)$, which would correspond to the fourth peak of $u_{out}(t)$ in a traditional $u_{out}(t)$ curve. In other words, the value that is returned by our algorithm is not β_- as we define it in the schematic waveforms of Fig. 2. Again, this is not of major

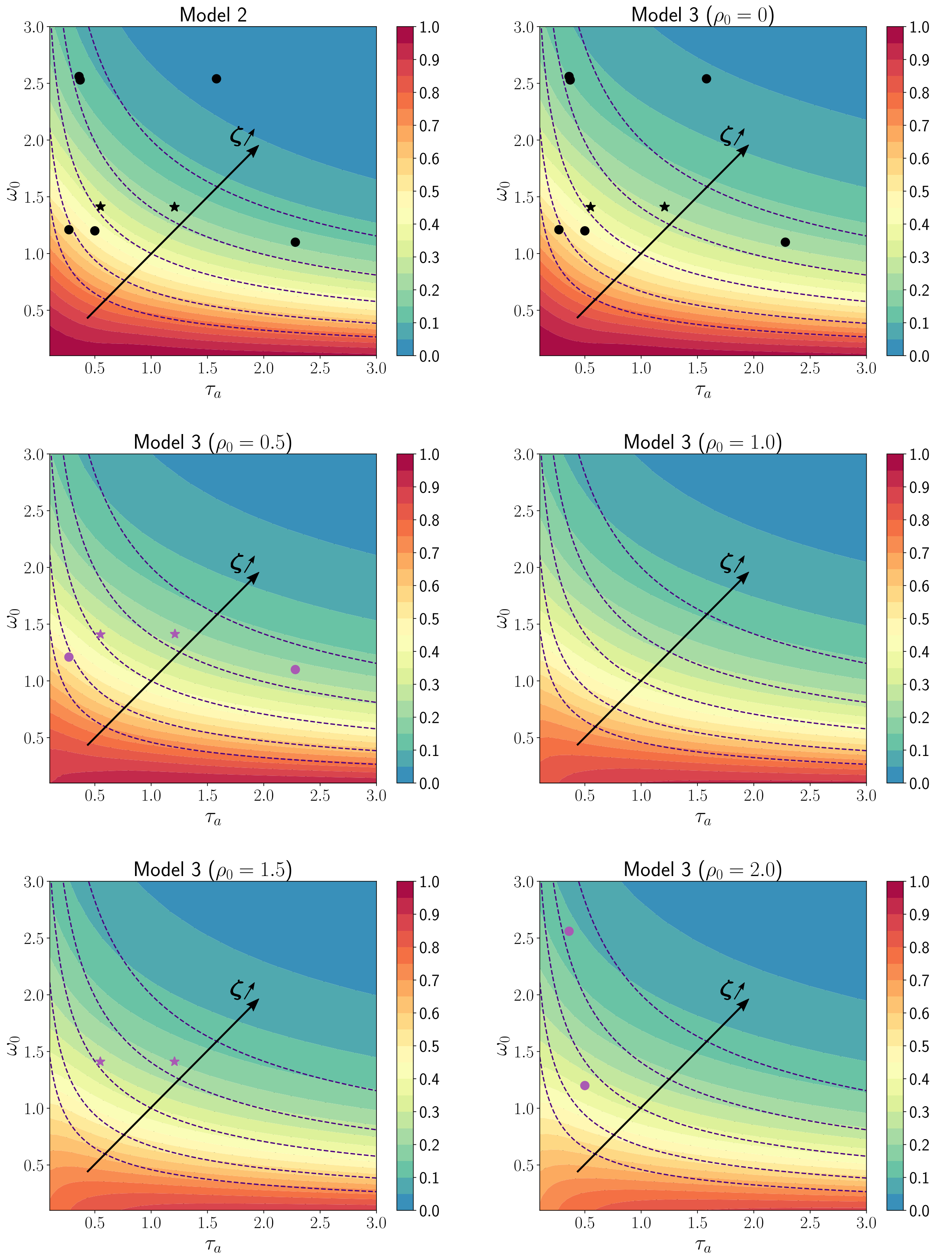

FIG. 11. Comparison of the $(\omega_0 - \tau_a)$ maps of the value of the multiplication efficiency β_+ related to the amplitude of the first peak of $\beta(t)$ between Bichenkov's model and our model for several values of the loss parameter ρ_0. Dots represent spiral generators configurations found in the literature and stars represent VIG made in our lab for the experimental validation of our model. Black symbols represent the location of each configuration when neglecting resistive losses, *i.e.* if $\rho_0 = 0$.
The dashed lines are isocurves of $\zeta = \frac{\tau_a}{\tau_p} = \frac{L_s}{L_s + L_{outer}}$, the values are $\zeta = \frac{1}{20}, \zeta = \frac{1}{10}, \zeta = \frac{1}{5}, \zeta = \frac{1}{3}$ and $\zeta = \frac{1}{2}$.

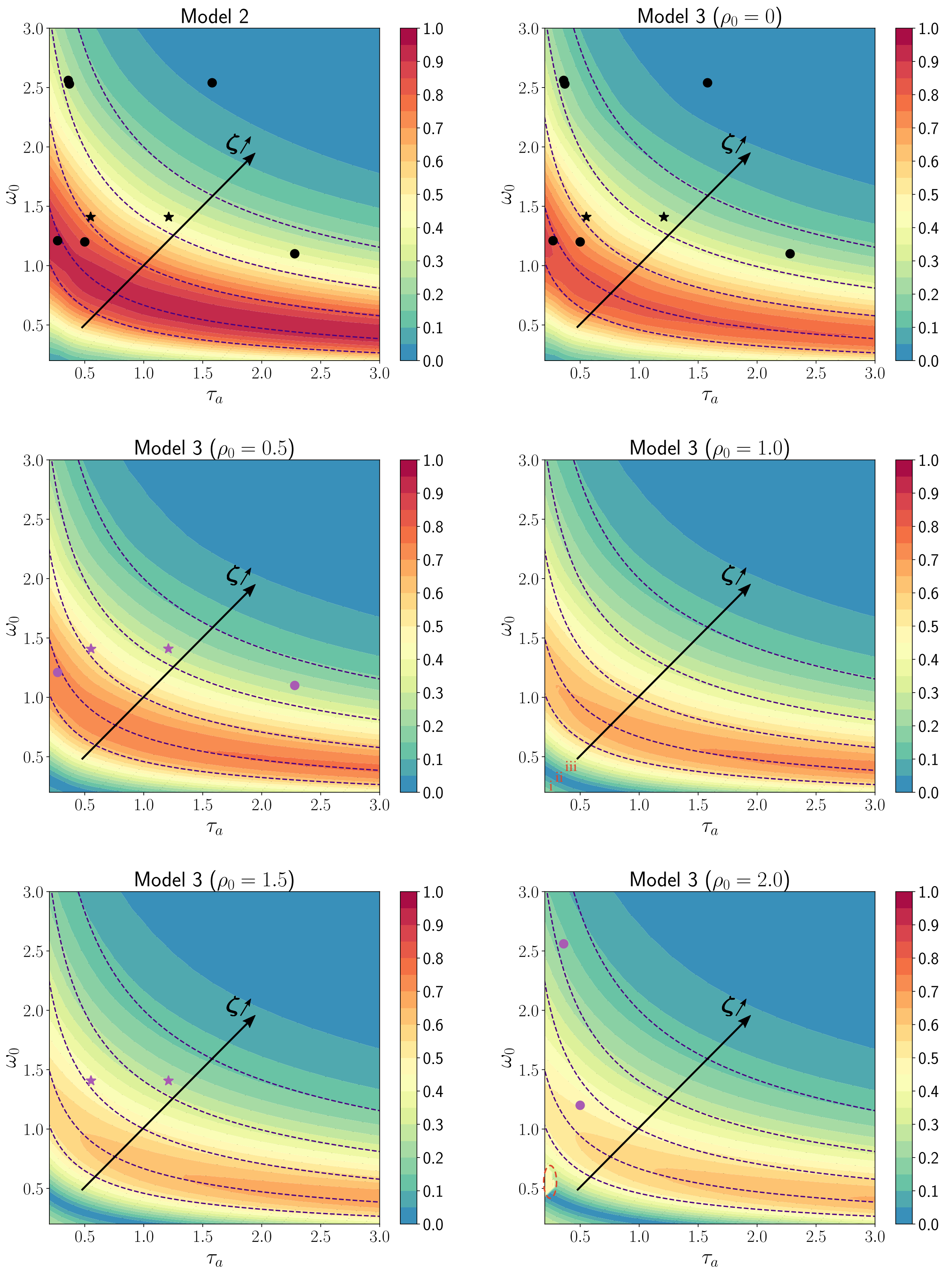

FIG. 12. Comparison of the $(\omega_0 - \tau_a)$ maps of the value of the multiplication efficiency β_- related to the amplitude of the second peak of $\beta(t)$ between Bichenkov's model and our model for several values of the loss parameter ρ_0. Dots represent spiral generators configurations found in the literature and stars represent VIG made in our lab for the experimental validation of our model. Black symbols represent the location of each configuration when neglecting resistive losses, *i.e.* if $\rho_0 = 0$.
The dashed lines are isocurves of $\zeta = \frac{\tau_a}{\tau_p} = \frac{L_s}{L_s + L_{outer}}$, the values are $\zeta = \frac{1}{20}, \zeta = \frac{1}{10}, \zeta = \frac{1}{5}, \zeta = \frac{1}{3}$ and $\zeta = \frac{1}{2}$.

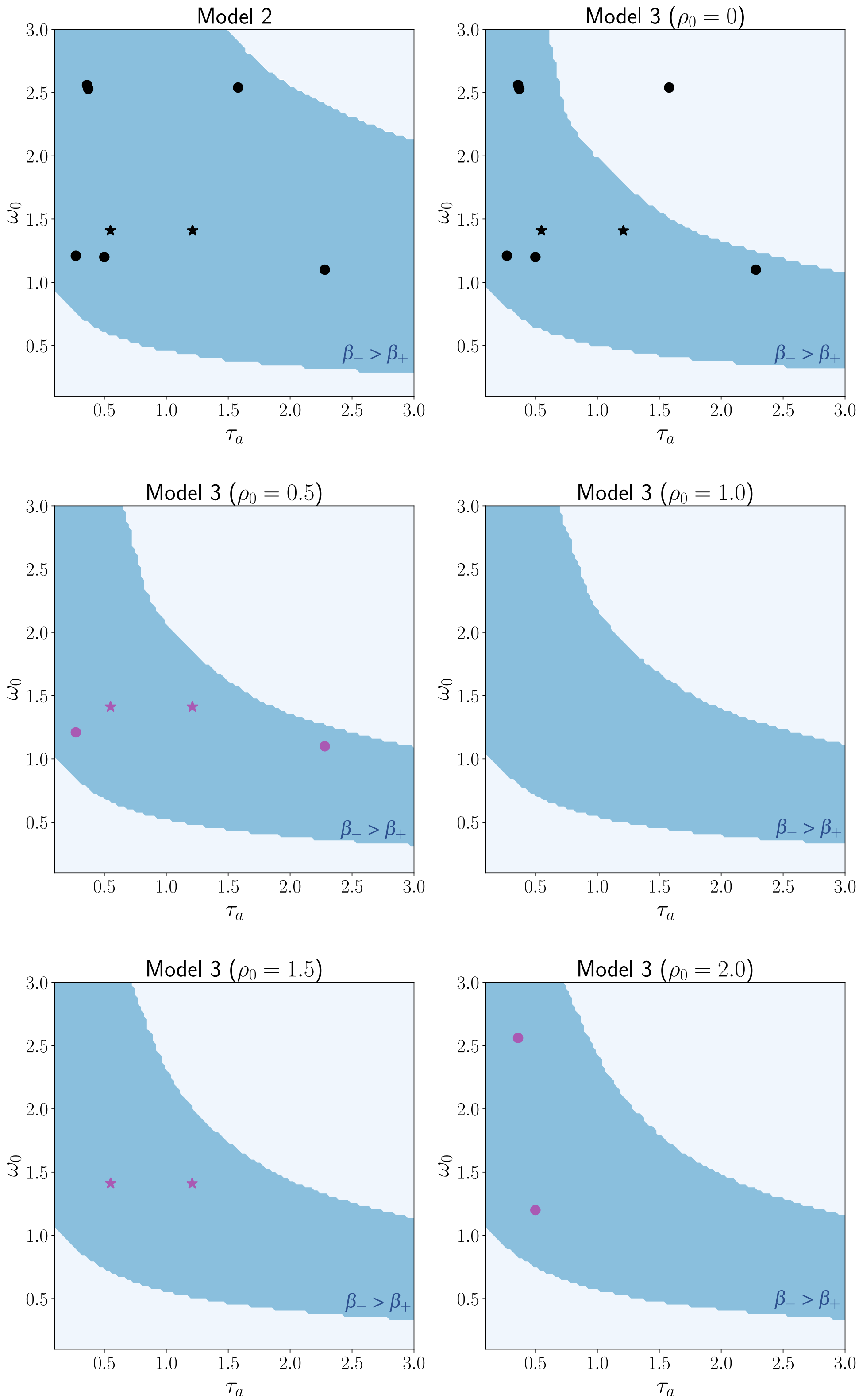

FIG. 13. Comparison of the multiplication efficiencies of the first and second peak of the output voltage. The blue regions of the $(\omega_0 - \tau_a)$ maps corresponds to VIGs configurations for which the absolute value of the amplitude of the second peak of $u_{out}(t)$ is higher than for the first peak, *i.e.* for which $\beta_- > \beta_+$. Dots represents spiral generators configurations found in the literature and stars represents VIG configurations made in our lab for the experimental validation of our model. Black symbols represent the location of each configuration when neglecting resistive losses, *i.e.* if $\rho_0 = 0$.

importance as it corresponds to regions of the $(\omega_0 - \tau_a)$ maps that are unlikely to be obtained in practice.

Comparison of the maps of β_+ and β_-

Fig. 13 shows a comparison of values of β_+ and β_-. The blue region is the region where the second peak of $u_{out}(t)$ offers higher multiplication efficiencies than the first peak. This region is almost independent of ρ_0 but strongly depends on the model that is used for the prediction. With Model 2, the region where $\beta_- > \beta_+$ is significantly larger than with Model 3. This result is in agreement with the conclusions taken from the β_+ and β_- maps discussed earlier as it was observed that Model 2 predicts higher values of β_- than Model 3 but almost similar values of β_+. It can also be seen in Fig. 13 that most dots and stars are located in the blue region. This gives evidence that most existing configurations of VIGs are actually located in the region where the second peak gives a higher multiplication efficiency than the first one.

V. CONCLUSION

In this paper, we provided a new dimensionless transfer function allowing to predict the analytical expression, in the Laplace domain, of the output voltage of a vector inversion generator. This model was obtained using the framework proposed Rühl and Herziger[17] in 1980 and by inserting in this framework the corrections proposed by Bichenkov *et al.*[18] in 2007 and adding two additional features: the crosstalk between i_a and i_p in the switch, and more importantly, resistive losses as suggested by Yan *et al.*[16], introducing a new dimensionless parameter ρ_0.

We validated our model by comparing the predictions of $\beta(t) = \frac{u_{out}(t)}{2Nu_0}$ given by our model with experimental measurements and with the predictions provided by other existing transfer functions[17,18]. The set of experiments allowed to evaluate the effect of the switch inductance by adding coils with different number of turns in series with a perfect mechanical switch. It also allowed to assess the impact of resistive losses by performing the experiments at different temperatures, *i.e.* by changing the value of the conductivity of the conductors. Results showed that our new transfer function allows better predictions of $u_{out}(t)$, both in terms of amplitude and timings, compared to formerly published transfer functions[17,18]. We also showed that the difference in amplitude mainly results from the assumption that there are no resistive losses in the other transfer functions and that the difference in timings is a consequence of neglecting the interactions between both currents near the switch.

Using numerical Laplace transforms, one can use our $B(p)$ transfer function (Eqs. 8 to 12) to estimate time evolutions of $\beta(t)$. The transfer function we propose contains the following dimensionless parameters, listed by order of importance:

1. **Essential parameters:** the following parameters are sufficient to obtain $u_{out}(t)$ prediction curves:
   - $\tau_a = \frac{L_s}{Z_0 T}$ represents the rise time of the active waveguide. It should be as low as possible, meaning that the inductance of the switch L_s should be minimized.
   - $\omega_0 = \frac{T}{\sqrt{LC}}$ represents the LC behavior of the spiral generator. This parameter should also be minimized, meaning that the resonance frequency of the spiral itself should be above the equivalent frequency of the voltage multiplication phenomenon. This criterion can be fulfilled by increasing the mean diameter of by inserting a magnetic material, increasing the value of L without affecting other parameters.
   - $\rho_0 = \frac{R'T}{L'}$ represents the resistive losses of the conductors. This parameter must also be minimized. Increasing the number of turns N results in a decrease of the absolute value of $\beta(t)$. In the expression $u_{out}(t) = 2N\beta(t)u_0$, $u_{out}(t)$ does not actually increase linearly with N.
   - $\tau = \frac{T}{ZC}$ represents the fact that a load of Laplace impedance Z is connected at the output of the spiral. Note that Z includes also the impedance of a measurement device when used. When no load is connected at the output of the spiral generator, this parameter is equal to zero and has no effect on $u_{out}(t)$.
2. **Useful for deeper understanding of spiral generators:** the following set of parameters are other ways to express the previously mentioned parameters but allow a better understanding of the physics happening in the voltage multiplication phenomenon:
   - $\tau_p = \frac{L_s + L_{outer}}{Z_0 T}$ represents the rise time of the passive waveguide. As the discharge of the passive waveguide deteriorates the output voltage multiplication phenomenon, this rise time should be as high as possible, so τ_p should be maximized. This parameter is not essential because it is a combination of τ_a and ω_0 ($\tau_p = \tau_a + \frac{4}{\omega_0^2}$) but it allows a better understanding of why ω_0 should be minimized. For a given value of τ_a, increasing τ_p means increasing L_{outer}, which can be achieved by increasing the mean diameter of the spiral or by inserting a magnetic material.
   - $\zeta = \frac{\tau_a}{\tau_p} = \frac{L_s}{L_s + L_{outer}}$ is another parameter that allows to compare the rise times of both waveguides. In the light of what was explained above, ζ should be minimised.
3. **Practically unimportant parameters:** these last two parameters appear in the mathematical development but can often by assumed to be equal to zero. They should only be considered if a very accurate prediction is desired:

- $\rho_a = \frac{R_s}{\sqrt{\frac{L'}{C'}}}$ represents the resistive losses of the switch.
- $\rho_p = \frac{R_s+R_{outer}}{\sqrt{\frac{L'}{C'}}}$ represents the resistive losses of the outer turn of the spiral generator.

Using our model, we generated several $(\omega_0 - \tau_a)$ maps of the predicted values of β_+ and β_+ for different values of ρ_0. These $(\omega_0 - \tau_a)$ maps allow someone to predict the values of β_+ and β_- knowing only the essential dimensionless parameters (these maps assume that no load is connected at the output of the spiral generator). These maps also made it possible to define a region where the amplitude of the second peak of $u_{out}(t)$ exceeds the first one.

ACKNOWLEDGMENTS

This work was funded through the Win2Wal program financed by the DGO6 department of the *Région Wallonne* (convention 2110062).

DATA AVAILABILITY STATEMENT

The data that support the findings of this study are available from the corresponding author upon reasonable request.

[1] W. Feng, P. Rao, S. Nimbalkar, Q. Chen, J. Cui, and P. Ouyang, "The Utilization of a Coupled Electro-Thermal-Mechanical Model of High-Voltage Electric Pulse on Rock Fracture," Materials **16**, 1693 (2023).

[2] B. Zhu, H. Su, Z. Fang, G. Wu, and X. Wei, "Development of a High-Voltage Pulsed Electric Field Sterilization Power Supply Using a New Topology Circuit," Energies **16**, 2741 (2023).

[3] E. I. Pal'chikov, A. V. Dolgikh, V. V. Klypin, A. M. Ryabchun, and M. S. Samoylenko, "Pulse X-ray Device Based on a Combined Spiral Generator," Journal of Applied Mechanics and Technical Physics **60**, 586–591 (2019).

[4] I. Lavrinovich, A. I. Gusev, S. Bland, A. S. de Ferron, L. Pécastaing, S. Parker, J. Yan, and B. M. Novac, "2-kV Thyristor Triggered in Impact-Ionization Wave Mode by a Solid-State Spiral Generator," IEEE Transactions on Plasma Science **50**, 3443–3451 (2022), conference Name: IEEE Transactions on Plasma Science.

[5] J.-H. Kim, M.-H. Ryu, B.-D. Min, S. Shenderey, Jong-Soo Kim, and Geun-Hie Rim, "High voltage pulse power supply using Marx generator & solid-state switches," in *31st Annual Conference of IEEE Industrial Electronics Society, 2005. IECON 2005.* (IEEE, Raleigh, NC, USA, 2005) p. 4 pp.

[6] L. Pecastaing, A. Ferron, M. RIVALETTO, B. CASSANY, B. Cadilhon, P. MODIN, and M. TEBOUL, "Compact self Marx generator with integrated PFL for an ultra-wideband source," Journal- Korean Physical Society **59**, 3463–3467 (2011).

[7] J. Li, X. Zhong, J. Li, Z. Liang, W. Chen, Z. Li, and T. Li, "Theoretical Analysis and Experimental Study on an Avalanche Transistor-Based Marx Generator," IEEE Transactions on Plasma Science **43**, 3399–3405 (2015).

[8] Y. S. Jin, S. W. Lim, C. H. Cho, J. S. Kim, Y. B. Kim, S. H. Lee, and Y. Roh, "High voltage ultrawide band pulse generator using Blumlein pulse forming line," Review of Scientific Instruments **83**, 044704 (2012).

[9] J. J. Coogan, F. Davanloo, and C. B. Collins, "Production of high-energy photons from flash x-ray sources powered by stacked Blumlein generators," Review of Scientific Instruments **61**, 1448–1456 (1990).

[10] S. Katsuki, D. Takano, T. Namihira, H. Akiyama, and T. Majima, "Repetitive operation of water-filled Blumlein generator," Review of Scientific Instruments **72**, 2759–2763 (2001).

[11] F. Davanloo, C. Collins, and F. Agee, "High-power, repetitive-stacked Blumlein pulsers commutated by a single switching element," IEEE Transactions on Plasma Science **26**, 1463–1475 (1998).

[12] R. Fitch and V. Howell, "Novel principle of transient high-voltage generation," Proceedings of the Institution of Electrical Engineers **111**, 849 (1964).

[13] R. Fitch and V. Howell, "Pulse generator," (U.S. Patent 3 289 015, Nov. 1966).

[14] J. Rice, R. Gripshover, M. Rose, and C. Van Wagoner, "Spiral line oscillator," (U.S. Patent 4 217 468, Aug. 1980).

[15] A. Kloss, B. Schalk, and S. Walter, "High voltage pulse generator and high-pressure discharge lamp having such a generator," (E.U. Patent 2 151 008 B1, Jun. 2012).

[16] J. Yan, S. Parker, and S. Bland, "An Investigation Into High-Voltage Spiral Generators Utilizing Thyristor Input Switches," IEEE Transactions on Power Electronics **36**, 10005–10019 (2021).

[17] F. Rühl and G. Herziger, "Analysis of the spiral generator," Review of Scientific Instruments **51**, 1541–1547 (1980).

[18] E. I. Bichenkov, E. I. Palchikov, A. M. Ryabchun, and T. Y. Bashkatov, "On the refinement of the theoretical model for a high-voltage spiral generator," Technical Physics **52**, 1597–1603 (2007).

[19] E. I. Pal'chikov, A. M. Ryabchun, and I. Y. Krasnikov, "Modified spiral high-voltage generator for feeding a pulsed X-ray apparatus," Technical Physics **57**, 292–301 (2012).

[20] H. Stehfest, "Algorithm 368: Numerical inversion of Laplace transforms [D5]," Communications of the ACM **13**, 47–49 (1970).

[21] T. H. G. Megson, "Chapter 16 - Analysis of Statically Indeterminate Structures," in *Structural and Stress Analysis (Third Edition)*, edited by T. H. G. Megson (Butterworth-Heinemann, Boston, 2014) pp. 489–570.

[22] MulticompPro, "Polyimide film tapes - non-adhesive," (MP700316 Datasheet , Jun. 2022).

[23] Keith and Henney, *Radio Engineering Handbook* (McGraw-Hill Book Company, Inc., 1963).

[24] E. B. Rosa and F. W. Grover, *Formulas and Tables for the calculation of mutual and self inductances (revisited)* (Scientific Papers of the Bureau of Standards, 1916).

[25] M. Rose, Z. Shotts, and Z. Roberts, "High Efficiency Compact High Voltage Vector Inversion Generators," in *2005 IEEE Pulsed Power Conference* (IEEE, Monterey, CA, USA, 2005) pp. 1207–1210.

[26] P. G. Pouraimis, A. P. Platis, J. M. Koutsoubis, and C. X. Manasis, "A Compact High-Voltage, Nanosecond Pulse Generator for Triggering Applications," in *2018 IEEE International Conference on High Voltage Engineering and Application (ICHVE)* (IEEE, ATHENS, Greece, 2018) pp. 1–4.

[27] C. Brau, J. L. Raybun, J. B. Dodge, and F. M. Gilman, "Simple, pulsed, electron beam gun," Review of Scientific Instruments **48**, 1154–1160 (1977).

Appendix A: Re-obtaining Rühl and Herziger transfer function

In this section, we re-do the development proposed in the article of Rühl and Herziger[17] and try to give some clarifications about how they obtained their results. In the model they propose, a magnetic approach of the vector inversion generator is proposed. As there are currents circulating in loops inside the spiral, a voltage U_{ind} is induced in each turn. The active conductor consisting of N turns, one has: $U_{out} = NU_{ind}$. As each turn is considered to see the same magnetic flux, one can deduce the first assumption: the magnetic coupling is equal to 1.
The next step in their paper is to list all the currents circulating in loops, *i.e.* the currents generating a magnetic flux:

- Circulating currents between layers reaching the active conductor at location x: $j_a(x)$ [A/m],
- Circulating currents between layers reaching the passive conductor at location x: $j_p(x)$ [A/m],
- The current in the load, circulating through the N turns of the active conductor: i_z [A].

In this definition, x is defined as the curvilinear abscissa along the spiral, with $x = 0$ being the location of the switch, $x = nl$ the end of the n-th turn and $x = x_{max} = Nl$ the center of the spiral, near the load.

Using Maxwell law of induction with the previously mentioned currents, one obtains:

$$U_{ind} = -sL_{turn}\left[NI_z + \int_0^{Nl} J_a(x)dx + \int_0^{Nl} J_p(x)dx\right]. \quad \text{(A1)}$$

The next equations proposed in their original article seemed to have some typos. The two following equations are a corrected version:

$$J_p(x-l) + 2J_a(x) + J_p(x) - \frac{\partial I_a(x)}{\partial x} - \frac{\partial I_p(x)}{\partial x} = sC'U_{ind}, \quad \text{(A2)}$$

$$J_a(x) + 2J_p(x) + J_a(x+l) + \frac{\partial I_a(x+l)}{\partial x} + \frac{\partial I_p(x)}{\partial x} = sC'U_{ind}. \quad \text{(A3)}$$

To understand where these relations come from, let us split the currents generating a magnetic flux as follows: the ones flowing through the active waveguide and the ones flowing through the passive waveguide, as illustrated in Fig. 14a.

- <u>Currents flowing across the active waveguide:</u> let us enumerate all the circulating currents flowing in the active waveguide along a radial portion of length dx:
  - Active waveguide: From the telegrapher's equations, a current $\frac{-\partial I_a(x)}{\partial x}dx$ flows in the parallel branch of a cell of length dx,
  - Passive waveguide: generates no current across the active conductor,
  - Circulating current reaching the active line at location x: $J_a(x)dx$,
  - Circulating current reaching the passive line at location $x-l$: $J_p(x-l)dx$.

As the active and passive waveguides have the same dimensions and physical properties, these currents will generate a voltage $\frac{U_{ind}}{2}$. It yields the following relation using Ohm's law:

$$sC'dx\frac{U_{ind}}{2} = J_a(x)dx + J_p(x-l)dx - \frac{\partial I_a(x)}{\partial x}dx. \quad \text{(A4)}$$

- <u>Currents flowing across the passive waveguide:</u> let us enumerate all the circulating currents flowing in the passive waveguide along a radial portion of length dx:
  - Active waveguide: generates no current across the passive waveguide,
  - Passive waveguide: From the telegrapher's equations, a current $\frac{-\partial I_p(x)}{\partial x}dx$ flows in the parallel branch of a cell of length dx,
  - Circulating current reaching the active line at location x: $J_a(x)dx$,
  - Circulating current reaching the passive line at location x: $J_p(x)dx$.

These currents will also generate a voltage $\frac{U_{ind}}{2}$. Using Ohm's law, it gives:

$$sC'dx\frac{U_{ind}}{2} = J_a(x)dx + J_p(x)dx - \frac{\partial I_p(x)}{\partial x}dx. \quad \text{(A5)}$$

Summing Eqs. A4 and A5 and dividing by dx allows to retrieve Eq. A2.

A similar reasoning with currents balances but one half turn upwards, as illustrated in Fig. 14b allows to retrieve Eq. A3. One can then add up Eqs. A2 and A3 allows to obtain:

$$\begin{aligned}2sC'U_{ind} = {} & 3J_p + 3J_a + J_p(x-l) + J_a(x+l) \\ & - \frac{\partial I_a(x)}{\partial x} - 2\frac{\partial I_p}{\partial x} - \frac{\partial I_a(x+l)}{\partial x}.\end{aligned} \quad \text{(A6)}$$

This equation is then integrated from $x = 0$ to $x = Nl$. One can notice that $J_a(x) = 0$ and $J_p(x) = 0$ for $x < 0$ and $x > (N-1)l$. The same applies for waveguide currents: $I_a(x) = 0$ and $\frac{\partial I_a(x)}{\partial x} = 0$ if $x < 0$ and $x > Nl$ and $I_p(x) = 0$ and $\frac{\partial I_p(x)}{\partial x} = 0$ if $x < 0$ and $x > (N-1)l$.

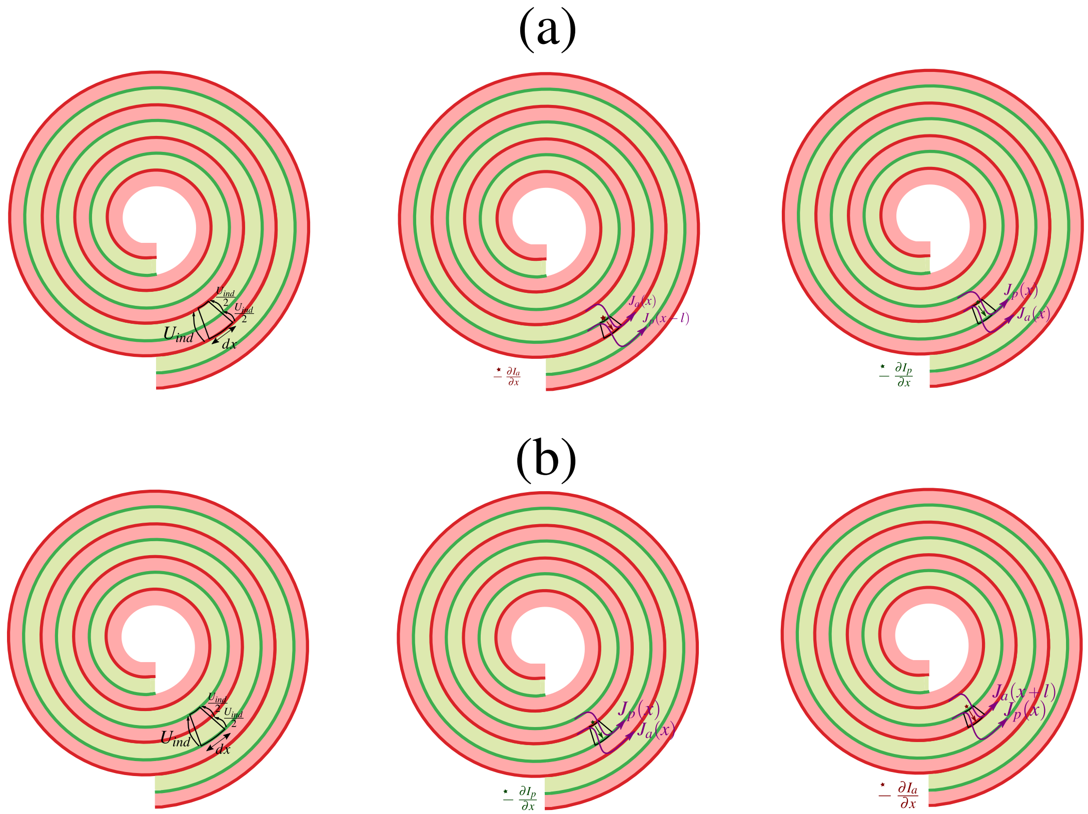

FIG. 14. Currents flowing through a portion dx of the active and passive waveguide at location x. A voltage $U_{ind}/2$ is generated on each waveguide. (a) Current balance to obtain Eq. A2. (b) Current balance to obtain Eq. A3.

These considerations allow to write:

$$\begin{aligned}
\int_0^{Nl} J_p(x-l)dx &= \int_{-l}^{(N-1)l} J_p(x)\,dx = \int_0^{Nl} J_p(x)\,dx,\\
\int_0^{Nl} J_a(x+l)dx &= \int_l^{(N+1)l} J_a(x)\,dx\\
&= \int_0^{Nl} J_a(x)\,dx - \int_0^{l} J_a(x)\,dx,\\
\int_0^{Nl} \frac{\partial I_a(x+l)}{\partial x}dx &= \int_l^{(N+1)l} \frac{\partial I_a(x)}{\partial x}dx\\
&= I_a(x=Nl) - I_a(x=0) - \int_0^{l} \frac{\partial I_a(x)}{\partial x}dx\\
&= -I_s - \int_0^{l} \frac{\partial I_a(x)}{\partial x}dx.
\end{aligned}$$

The main error committed by Rühl and Herziger lies in this step where they wrongly state that $I_a(x=0) = I_s$, hence neglecting current in the passive waveguide.

Including these integrals in Eq. A6 and dividing by 2 yields:

$$\begin{aligned}
sC'Nl\,U_{ind} =& 2\int_0^{Nl} J_a(x)\,dx + 2\int_0^{Nl} J_p(x)\,dx\\
&-\frac{1}{2}\int_0^{l}\left(J_a(x) - \frac{\partial I_a(x)}{\partial x}\right)dx - I_s.
\end{aligned}$$

Neglecting the integral ranging from $x=0$ to $x=l$ and rearranging the terms leads to:

$$\int_0^{Nl} J_a\,dx + \int_0^{Nl} J_p\,dx = \frac{1}{2}\left(sC'NlU_{ind} + I_s\right).$$

Injecting this relation in A1 gives:

$$U_{ind} = -sL_{turn}\left[NI_z + \frac{1}{2}sC'NlU_{ind} + \frac{1}{2}I_s\right].$$

After replacing $U_{out} = NU_{ind}$ and $I_z = \frac{U_{out}}{Z}$, one obtains:

$$U_{out} = \frac{-\frac{1}{2}sI_s}{\frac{1}{NL_{turn}} + \frac{1}{2}s^2C'l + \frac{sN}{Z}}.$$

One can then define $L = N^2L_{turn}$ and $C = \frac{C'l}{2N}$, leading to the transfer function proposed by Rühl and Herziger:

$$U_{out}(s) = \frac{-sI_s}{2NC\left(s^2 + \frac{s}{ZC} + \frac{1}{LC}\right)}. \tag{A7}$$

The next step is to use the waveguide equations to find a way to express I_s as a function of U_{out}. Using Ohm's law on a portion dx of the active waveguide gives:

$$sC'dxU_a(x,s) = -\frac{\partial I_a(x,s)}{\partial x}dx + J_a(x)dx + J_p(x-l)dx. \tag{A8}$$

Assuming that the waveguide acts as the undisturbed waveguide, one can write:

$$I_a(x,s) = I_+e^{-\gamma x} - I_-e^{\gamma x},$$

with $\gamma = s\sqrt{L'C'}$ for a lossless waveguide. Using the boundary condition $I_a(Nl) = 0$ allows to re-write the previous expression as:

$$I_a(x,s) = I_+\left(e^{-\gamma x} - e^{\gamma(x-2Nl)}\right).$$

The next step is to inject this expression of $I_a(x,s)$ in equation A8. The latter also contains $J_a(x)$ and $J_p(x)$ terms which are unknown quantities. To overcome this issue, it is assumed that the space derivative of circulating currents is negligible and replace them by their mean value:

$$J_a(x) \simeq \frac{1}{Nl}\int_0^{Nl} J_a(x)\,dx,$$
$$J_p(x-l) \simeq \frac{1}{Nl}\int_0^{Nl} J_p(x-l)\,dx = \frac{1}{Nl}\int_0^{Nl} J_p(x)\,dx.$$

One can then re-use equation A1 and try to make these $J_a(x)$ and $J_p(x)$ integrals also appear:

$$\frac{U_{out}}{N} = -sL_{turn}\left[NI_z + \int_0^{Nl} J_a\,dx + \int_0^{Nl} J_p\,dx\right]$$
$$\Leftrightarrow \int_0^{Nl} J_a\,dx + \int_0^{Nl} J_p\,dx = \frac{-1}{sL_{turn}}\frac{U_{out}}{sN} - N\frac{U_{out}}{Z}$$
$$\Leftrightarrow \int_0^{Nl} J_a\,dx + \int_0^{Nl} J_p\,dx \simeq -NU_{out}\left[\frac{1}{sL} + \frac{1}{Z}\right].$$

Which means that the sum of the mean integral values of circulating currents can be replaced as follows:

$$\frac{1}{Nl}\int_0^{Nl} J_a\,dx + \frac{1}{Nl}\int_0^{Nl} J_p\,dx \simeq \frac{-U_{out}}{l}\left[\frac{1}{sL} + \frac{1}{Z}\right].$$

This last relation can be injected in equation A8 and one can then solve for the I_+ constant:

$$sC'U_a(x,s) = -\frac{\partial I_a(x,s)}{\partial x} + J_a(x) + J_p(x-l)$$
$$\Leftrightarrow sC'U_a(x,s) = I_+\left[\gamma e^{-\gamma x} + \gamma e^{\gamma(x-2Nl)}\right] - \frac{U_{out}}{l}\left[\frac{1}{sL} + \frac{1}{Z}\right]$$
$$\Leftrightarrow U_a(x,s) = Z_0 I_+\left[e^{-\gamma x} + e^{\gamma(x-2Nl)}\right] - \frac{U_{out}}{sC'l}\left[\frac{1}{sL} + \frac{1}{Z}\right].$$

where $Z_0 = \sqrt{\frac{L'}{C'}} = \frac{\gamma}{sC'}$ is the characteristic impedance of a lossless waveguide. Using the boundary conditions at $x = 0$:

$$U_a(0,s) = \frac{u_0}{s} - Z_s I_s = \frac{u_0}{s} - Z_s I_a(0,s),$$

allows to solve for I_+:

$$I_+ = \frac{\frac{u_0}{s} + \frac{U_{out}}{sC2N}\left(\frac{1}{sL} + \frac{1}{Z}\right)}{\left(1 - e^{-sT}\right)\left(Z_0\coth\left(\frac{sT}{2}\right) + Z_s\right)},$$

which finally makes it possible to replace $I_s = I_a(x = 0)$ in the transfer function U_{out}:

$$I_s = I_+\left(1 - e^{-2\gamma Nl}\right) = I_+\left(1 - e^{-sT}\right)$$
$$\Leftrightarrow I_s = \frac{\frac{u_0}{s}}{\left(Z_0\coth\left(\frac{sT}{2}\right) + Z_s\right)} + \frac{\frac{U_{out}}{2Ns}\left(\frac{1}{sLC} + \frac{1}{ZC}\right)}{\left(Z_0\coth\left(\frac{sT}{2}\right) + Z_s\right)}.$$

Calling $A(s) = \frac{1}{s}\frac{1}{\left(Z_0\coth\left(\frac{sT}{2}\right) + sL_s\right)}$, one can find the expression of the output voltage $U_{out}(s)$ by re-using Eq. A7:

$$U_{out}(s) = -\frac{su_0A(s) + \frac{sU_{out}}{2N}\left(\frac{1}{sLC} + \frac{1}{ZC}\right)A(s)}{2NC\left(s^2 + \frac{1}{ZC}s + \frac{1}{LC}\right)}$$
$$\Leftrightarrow U_{out}(s) = -\frac{sA(s)u_0}{2NCs^2 + \left(2NC - \frac{A(s)}{2N}\right)\left(\frac{s}{ZC} + \frac{1}{LC}\right)}. \tag{A9}$$

The final step is to make the following dimensionless parameters appear:

- $p = sT$ the Laplace variable,
- $\tau_a = \frac{L_s}{Z_0T}$ accounting for the effects of the switch,
- $\tau = \frac{T}{ZC}$ accounting for the effects of the output load,
- $\omega_0 = \frac{T}{\sqrt{LC}}$ the dimensionless resonance frequency .

With this change of variable, $A(s)$ becomes $A(p)$:

$$A(s) = \frac{1}{s}\frac{1}{Z_0\coth\left(\frac{sT}{2}\right) + sL_s} = \frac{1}{Z_0}\frac{1}{s\coth\left(\frac{sT}{2}\right) + \frac{s^2L_s}{Z_0}}$$
$$= \frac{1}{Z_0}\frac{1}{\frac{sT}{T}\coth\left(\frac{sT}{2}\right) + \frac{s^2L_sT}{Z_0T}} = \frac{T}{Z_0}A(p).$$

To simplify calculations, one can use the following relation:

$$\frac{T}{Z_0} = \frac{2Nl\sqrt{L'C'}}{\sqrt{\frac{L'}{C'}}} = 2NlC' = (2N)^2C.$$

One then has:

$$U_{out}(s) = \frac{-su_0A(p)(2N)^2C}{2NCs^2 + \left(2NC - \frac{(2N)^2CA(p)}{2N}\right)\left(\frac{s}{ZC} + \frac{1}{LC}\right)}$$
$$\Leftrightarrow \frac{U_{out(p)}}{2Nu_0T} = \frac{1}{T}\frac{-sA(p)}{s^2 + (1 - A(p))\left(\frac{s}{ZC} + \frac{1}{LC}\right)}$$
$$\Leftrightarrow B(p) = \frac{1}{T^2}\frac{-pA(p)}{\frac{p^2}{T^2} + (1 - A(p))\left(\frac{\tau p}{T^2} + \frac{\omega_0^2}{T^2}\right)}. \tag{A10}$$

Which after cancellation of the T^2 terms is the final dimensionless transfer function provided in the article:

$$B_1(p) = \frac{U_{out}}{2Nu_0T} = \frac{-pA(p)}{p^2 + (1 - A(p))\left(\tau p + \omega_0^2\right)}, \qquad \text{(A11)}$$

with: $A(p) = \frac{1}{p\coth\left(\frac{p}{2}\right) + p^2\tau_a}$.

Appendix B: Our complete mathematical developments

1. Considering the discharge of the passive waveguide

In our model, we took the discharge of the passive waveguide into account. The difference when taking this discharge into account is in the boundary conditions at $x = 0$. The new set of boundary conditions is:

$$\begin{cases} U_a(x=0,s) &= \frac{u_0}{s} - Z_s I_s(s), \\ U_p(x=0,s) &= \frac{-u_0}{s} - Z_s I_s(s) - Z_{outer} I_p(x=0,s), \\ I_s(s) &= I_a(x=0,s) - I_p(x=0,s). \end{cases}$$

Let us first see how it affects the first transfer function given by Rühl and Herziger. When integrating the following relation from $x = 0$ to $x = Nl$:

$$2sC'U_{ind} = 3J_p + 3J_a + J_p(x-l) + J_a(x+l) - \frac{\partial I_a(x)}{\partial x} - 2\frac{\partial I_p}{\partial x} - \frac{\partial I_a(x+l)}{\partial x}.$$

the term $I_a(x=0)$ appeared. There is now a similar term for the passive line. The rest of the development being unchanged, the new transfer function is:

$$U_{out}(s) = \frac{-s\left(I_a(x=0) + I_p(x=0)\right)}{2NC\left(s^2 + \frac{s}{ZC} + \frac{1}{LC}\right)}. \qquad \text{(B1)}$$

One must now solve the wave equations in the active and passive waveguides to obtain an expression for the numerator. As before, let us assume that the waveguides act as undisturbed waveguides:

$$I_a(x,s) = I_{a+}\left(e^{-\gamma x} - e^{\gamma(x-2Nl)}\right),$$
$$I_p(x,s) = I_{p+}\left(e^{-\gamma x} - e^{\gamma(x-2Nl)}\right).$$

Similarly to what was done before, one must now find expressions for $U_a(x,s)$ and $U_p(x,s)$ by replacing the displacement currents by their mean value. For $U_a(x,s)$ it yields:

$$U_a(x,s) = Z_0 I_{a+}\left(e^{-\gamma x} + e^{\gamma(x-2Nl)}\right) - \frac{U_{out}}{C'l}\left(\frac{1}{sL} + \frac{1}{Z}\right)$$

For the sake if visibility, we define $U^*_{out} = \frac{U_{out}}{sC'l}\left(\frac{1}{sL} + \frac{1}{Z}\right)$. Doing the same for the passive waveguide finally gives the following set of equations:

$$U_a(x,s) = Z_0 I_{a+}\left(e^{-\gamma x} + e^{\gamma(x-2Nl)}\right) - \frac{U^*_{out}}{s},$$
$$U_p(x,s) = Z_0 I_{p+}\left(e^{-\gamma x} + e^{\gamma(x-2Nl)}\right) - \frac{U^*_{out}}{s}.$$

Using the boundary conditions at $x = 0$, one can obtain the following set of equations and solve for I_{a+} and I_{p+}:

$$\begin{aligned} Z_0 I_{a+}(1 + e^{-sT}) - \frac{U^*_{out}}{s} &= \frac{u_0}{s} - Z_s I_{a+}\left(1 - e^{-sT}\right) \qquad \text{(B2)} \\ &\quad + Z_s I_{p+}\left(1 - e^{-sT}\right), \\ Z_0 I_{p+}(1 + e^{-sT}) - \frac{U^*_{out}}{s} &= \frac{-u_0}{s} + Z_s I_{a+}\left(1 - e^{-sT}\right) \qquad \text{(B3)} \\ &\quad - (Z_s + Z_{outer}) I_{p+}\left(1 - e^{-sT}\right). \end{aligned}$$

From Eq. B2, one can obtain the following relation:

$$\begin{aligned} & I_{a+}\left(1 - e^{-sT}\right)\left[Z_0\coth\left(\tfrac{sT}{2}\right) + Z_s\right] \\ & \quad = \tfrac{u_0}{s} + \tfrac{U^*_{out}}{s} + Z_s I_{p+}\left(1 - e^{-sT}\right) \\ \Leftrightarrow \quad & I_{a+}\left(1 - e^{-sT}\right) = A(s)u_0 + A(s)U^*_{out} \\ & \qquad + sZ_s A(s) I_{p+}\left(1 - e^{-sT}\right), \qquad \text{(B4)} \end{aligned}$$

in which we define $A(s) = \frac{1}{s}\frac{1}{Z_0\coth\left(\frac{sT}{2}\right) + Z_s}$.

Injecting Eq. B4 in Eq. B3 gives:

$$\begin{aligned} & I_{p+}\left[Z_0\left(1 + e^{-sT}\right) + (Z_s + Z_{outer})\left(1 - e^{-sT}\right)\right] = \\ & \quad \tfrac{-u_0}{s} + \tfrac{U^*_{out}}{s} + Z_s A(s) u_0 + Z_s A(s) U^*_{out} \\ & \quad + sZ_s^2 A(s) I_{p+}\left(1 - e^{-sT}\right) \\ \Leftrightarrow & I_{p+}\left(1 - e^{-sT}\right)\left[Z_0\coth\left(\tfrac{sT}{2}\right) + (Z_s + Z_{outer}) - sZ_s^2 A(s)\right] \\ & \quad = u_0\left(\tfrac{-1}{s} + Z_s A(s)\right) + U^*_{out}\left(\tfrac{1}{s} + Z_s A(s)\right). \qquad \text{(B5)} \end{aligned}$$

Defining $P(s) = \frac{1}{s}\frac{1}{Z_0\coth\left(\frac{sT}{2}\right) + (Z_s + Z_{outer})}$ to simplify Eq. B5 yields:

$$\begin{aligned} I_{p+}\left(1 - e^{-sT}\right) &= \frac{u_0\left(\frac{-1}{s} + Z_s A(s)\right) + U^*_{out}\left(\frac{1}{s} + Z_s A(s)\right)}{\frac{1}{sP(s)} - sZ_s^2 A(s)} \\ \Leftrightarrow I_{p+}\left(1 - e^{-sT}\right) &= \frac{u_0\left[-P(s) + sZ_s A(s) P(s)\right]}{1 - Z_s^2 sA(s) sP(s)} \\ &\quad + \frac{U^*_{out}\left[P(s) + sZ_s A(s) P(s)\right]}{1 - Z_s^2 sA(s) sP(s)}, \qquad \text{(B6)} \end{aligned}$$

which allows to find an expression for I_{a+} by re-injecting Eq. B6 in Eq. B4:

$$\begin{aligned} I_{a+}\left(1 - e^{-sT}\right) = &\frac{u_0\left[A(s) - sZ_s A(s) P(s)\right]}{1 - Z_s^2 sA(s) sP(s)} \\ & + \frac{U^*_{out}\left[A(s) + sZ_s A(s) P(s)\right]}{1 - Z_s^2 sA(s) sP(s)}. \end{aligned}$$

With this, one can find a value for:

$$I_a(x=0)+I_p(x=0)=I_{a+}\left(1-e^{-sT}\right)+I_{p+}\left(1-e^{-sT}\right)$$

It gives:

$$\begin{aligned}I_a(x=0)+I_p(x=0)&=u_0\,\frac{A(s)-P(s)}{1-Z_s^2sA(s)sP(s)}\\&+U_{out}^*\,\frac{A(s)+P(s)+2sZ_sA(s)P(s)}{1-Z_s^2sA(s)sP(s)}\\&=u_0F(s)+U_{out}^*G(s).\end{aligned}\tag{B7}$$

Eq. B7 can be re-injected in Ruhl's modified equation of $U_{out}(s)$ (Eq. B1) to obtain the following transfer:

$$U_{out}(s)=\frac{-su_0F(s)}{2NCs^2+\left(2NC-\frac{G(s)}{2N}\right)\left(\frac{s}{ZC}+\frac{1}{LC}\right)}.\tag{B8}$$

The final step is to make dimensionless parameters appear in the transfer function. As we now considered a new physical phenomenon, we need to define a parameter related to the discharge of the passive waveguide: $\tau_p=\frac{L_s+L_{turn}}{Z_0T}$. This new parameter is related to the other ones by the following relation:

$$\begin{aligned}\tau_p&=\frac{L_s+L_{turn}}{Z_0T}\\\Leftrightarrow\tau_p&=\frac{L_s}{Z_0T}+\frac{\frac{L}{N^2}}{Z_0T}\\\Leftrightarrow\tau_p&=\tau_a+\frac{L}{T}\,\frac{1}{N^2\sqrt{\frac{L'}{C'}}}\\\Leftrightarrow\tau_p&=\tau_a+\frac{L}{T}\,\frac{\sqrt{C'}}{N^2\sqrt{L'}}\,\frac{\sqrt{C'}l}{\sqrt{C'}l}\,\frac{4}{4}\\\Leftrightarrow\tau_p&=\tau_a+\frac{L}{T}\,\frac{C'l}{2N}\,\frac{1}{2Nl\sqrt{L'C'}}4\\\Leftrightarrow\tau_p&=\tau_a+4\frac{LC}{T^2}\\\Leftrightarrow\tau_p&=\tau_a+\frac{4}{\omega_0^2}.\end{aligned}\tag{B9}$$

Let us now see how $F(s)$ and $G(s)$ can be rendered dimensionless:

$$\begin{aligned}F(s)&=\frac{A(s)-P(s)}{1-Z_s^2sA(s)sP(s)}\\&=\frac{\frac{T}{Z_0}\left(A(p)-P(p)\right)}{1-s^2(sL_s)^2\frac{T^2}{Z_0^2}A(p)P(p)}\\&=\frac{T}{Z_0}\,\frac{A(p)-P(p)}{1-s^4\frac{T^2}{Z_0^2}L_s^2A(p)P(p)}\\&=\frac{T}{Z_0}\,\frac{A(p)-P(p)}{1-p^4\tau_a^2A(p)P(p)}\\&=\frac{T}{Z_0}\,F(p),\\G(s)&=\frac{A(s)+P(s)+2sZ_sA(s)P(s)}{1-Z_s^2sA(s)sP(s)}=\frac{Num}{Denom},\\Num&=\frac{T}{Z_0}A(p)+\frac{T}{Z_0}P(p)-2ssL_s\frac{T^2}{Z_0^2}A(p)P(p)\\&=\frac{T}{Z_0}\left[A(p)+P(p)+2s^2L_s\frac{T}{Z_0}\frac{T}{T}A(p)P(p)\right]\\&=\frac{T}{Z_0}\left[A(p)+P(p)+2p^2\tau_aA(p)P(p)\right],\\Denom&=1-s^2(sL_s)^2\frac{T^2}{Z_0^2}A(p)P(p)\\&=1-p^4\tau_a^2A(p)P(p).\end{aligned}$$

In the end, the dimensionless form of the transfer function becomes:

$$B_3(p)=\frac{U_{out}}{2Nu_0T}=\frac{-pF(p)}{p^2+(1-G(p))\left(\tau p+\omega_0^2\right)}\tag{B10}$$

containing the following dimensionless functions:

$$A(p)=\frac{1}{p\coth\left(\frac{p}{2}\right)+p^2\tau_a},\tag{B11}$$

$$P(p)=\frac{1}{p\coth\left(\frac{p}{2}\right)+p^2\tau_p},\tag{B12}$$

$$F(p)=\frac{A(p)-P(p)}{1-p^4\tau_a^2A(p)P(p)},\tag{B13}$$

$$G(p)=\frac{A(p)+P(p)+2p^2\tau_aA(p)P(p)}{1-p^4\tau_a^2A(p)P(p)}.\tag{B14}$$

The transfer function proposed by Bichenkov *et al.* can be obtained with our approach by considering no current interaction in the switch. This is valid when $\tau_a<<\frac{4}{\omega^2}$. One then has the following set of boundary conditions:

$$\begin{cases}U_a(x=0,s)&=&\frac{u_0}{s}-Z_sI_a(x=0,s),\\U_p(x=0,s)&=&\frac{-u_0}{s}-(Z_s+Z_{outer-turn})I_p(x=0,s),\\I_s(s)&=&I_a(x=0,s)-I_p(x=0,s).\end{cases}$$

These conditions are easier to solve for I_{a+} and I_{a-}. Doing the algebra yields the following dimensionless transfer function:

$$B_2(p)=\frac{U_{out}}{2Nu_0T}=\frac{-p\left(A(p)-P(p)\right)}{p^2+\left[1-\left(A(p)+P(p)\right)\right]\left(\tau p+\omega_0^2\right)}.\tag{B15}$$

Note that Bichenkov *et al.* used a totally different approach, based on electric fields and voltages rather than a magnetic approach, but still obtained the exact same transfer function.

2. Considering resistive losses

Our major contribution to the modeling of VIGs is to make it possible to account for resistive losses. Resistive losses are present along the conductors and can be taken into account by means of a resistance per unit length R'. Our model neglects losses in the dielectric layer, but these losses could also be considered by also adding a conductance per unit length G' in the waveguide equations. One can also consider the resistance of the switch by adding resistive terms to $Z_s = sL_s + R_s$ and $Z_{outer} = sL_{outer} + R_{outer} = sL_{outer} + R'\pi D$. The resulting transfer function has a similar form as before:

$$\tilde{B}_3(p) = \frac{U_{out}}{2Nu_0T} = \frac{-p\tilde{F}(p)}{p^2 + \left(1-\tilde{G}(p)\right)\left(\tau p + \omega_0^2\right)}, \quad \text{(B16)}$$

where the tilde quantities denote the fact that they have been updated with additional terms to account for resistive losses.

The resistance per unit length of the conductors will only modify $A(s)$ and $P(s)$ as the wave equations are modified. The updated parameters of the waveguides are now:

- $\tilde{Z}_0 = \sqrt{\frac{R'+sL'}{sC'}} = \sqrt{\frac{L'}{C'}}\sqrt{1+\frac{R'}{sL'}}$,
- $\tilde{\gamma} = \sqrt{s^2L'C' + sR'C'} = s\sqrt{L'C'}\sqrt{1+\frac{R'}{sL'}}$,
- one still has the following relation: $\frac{\tilde{\gamma}}{sC'} = \tilde{Z}_0$.

Doing the algebra leads to the following waveguide current responses:

$$\begin{aligned}
\tilde{A}(s) &= \frac{1}{s\left[\tilde{Z}_0 \coth\left(\frac{sT}{2}\sqrt{1+\frac{R'}{sL'}}\right) + Z_s\right]} \\
&= \frac{1}{s\left[\sqrt{\frac{L'}{C'}}\cdot\sqrt{1+\frac{R'}{sL'}}\coth\left(\frac{sT}{2}\sqrt{1+\frac{R'}{sL'}}\right) + Z_s\right]}, \\
\tilde{P}(s) &= \frac{1}{s\left[\tilde{Z}_0 \coth\left(\frac{sT}{2}\sqrt{1+\frac{R'}{sL'}}\right) + (Z_s + Z_{outer})\right]} \\
&= \frac{1}{s\left[\sqrt{\frac{L'}{C'}}\cdot\sqrt{1+\frac{R'}{sL'}}\coth\left(\frac{sT}{2}\sqrt{1+\frac{R'}{sL'}}\right) + (Z_s + Z_{outer})\right]}.
\end{aligned}$$

As far as R_s and R_{outer} are concerned, these quantities will appear in all the parts of the developments that involves Z_s and Z_{outer}, that is in $A(s)$ and $P(s)$ but also in the $F(s)$ and $G(s)$ functions. Let us first focus on $A(s)$ and $P(s)$:

$$\tilde{A}(s) = \frac{1}{s\left[\sqrt{\frac{L'}{C'}}\cdot\sqrt{1+\frac{R'}{sL'}}\coth\left(\frac{sT}{2}\sqrt{1+\frac{R'}{sL'}}\right) + sL_s + R_s\right]},$$

which we can, as before, try to turn into a dimensionless expression:

$$\tilde{A}(s) = \frac{1}{\sqrt{\frac{L'}{C'}}} \cdot \frac{1}{s\sqrt{1+\frac{R'}{sL'}}\coth\left(\frac{sT}{2}\sqrt{1+\frac{R'}{sL'}}\right) + \frac{s^2L_s}{\sqrt{\frac{L'}{C'}}} + \frac{sR_s}{\sqrt{\frac{L'}{C'}}}},$$

which we can further simplify into:

$$\begin{aligned}
\tilde{A}(s) &= \frac{T}{\sqrt{\frac{L'}{C'}}} \frac{1}{p\sqrt{1+\frac{\rho_0}{p}}\coth\left(\frac{p}{2}\sqrt{1+\frac{\rho_0}{p}}\right) + p^2\tau_a + p\rho_a} \\
&= \frac{T}{\sqrt{\frac{L'}{C'}}} A(p),
\end{aligned}$$

with $\rho_0 = \frac{R'T}{L'}$, $\tau_a = \frac{L_s}{\sqrt{\frac{L'}{C'}}T}$ and $\rho_a = \frac{R_s}{\sqrt{\frac{L'}{C'}}}$.

A similar reasoning for $P(s)$ yields:

$$\begin{aligned}
\tilde{P}(s) &= \frac{T}{\sqrt{\frac{L'}{C'}}} \frac{1}{p\sqrt{1+\frac{\rho_0}{p}}\coth\left(\frac{p}{2}\sqrt{1+\frac{\rho_0}{p}}\right) + p^2\tau_p + p\rho_p} \\
&= \frac{T}{\sqrt{\frac{L'}{C'}}} \tilde{P}(p),
\end{aligned}$$

with $\tau_p = \frac{L_s+L_{outer}}{\sqrt{\frac{L'}{C'}}T}$ and $\rho_p = \frac{R_s+R_{outer}}{\sqrt{\frac{L'}{C'}}}$.

The remaining step is to see how resistive losses affect $F(s)$ and $G(s)$. $\tilde{F}(s) = \frac{\tilde{A}(s)-\tilde{P}(s)}{1-Z_s^2 s\tilde{A}(s)s\tilde{P}(s)} = \frac{Num}{Denom}$, the numerator is already dealt with as the expressions of $\tilde{A}(s)$ and $\tilde{P}(s)$ have just been established. One must only take care of the denominator of $\tilde{F}(s)$ to consider the change in Z_s:

$$\begin{aligned}
Denom &= 1 - Z_s^2 s\tilde{A}(s)s\tilde{P}(s) \\
&= 1 - \frac{T^2}{\frac{L'}{C'}} s^2 \left(sL_s + R_s\right)^2 \tilde{A}(p)\tilde{P}(p) \\
&= 1 - \frac{T^2}{\frac{L'}{C'}} s^2 \left(s^2L_s^2 + R_s^2 + 2sL_sR_s\right)\tilde{A}(p)\tilde{P}(p) \\
&= 1 - \left[\frac{s^2L_s^2T^2}{\frac{L'}{C'}} + \frac{s^2R_s^2T^2}{\frac{L'}{C'}} + \frac{2s^3L_sR_sT^2}{\frac{L'}{C'}}\right]\tilde{A}(p)\tilde{P}(p) \\
&= 1 - \left[p^4\tau_a^2 + 2p^3\rho_a\tau_a + p^2\rho_a\right]\tilde{A}(p)\tilde{P}(p).
\end{aligned}$$

And as $\tilde{G}(s) = \frac{\tilde{A}(s)+\tilde{P}(s)+2sZ_s\tilde{A}(s)\tilde{P}(s)}{1-Z_s^2 s\tilde{A}(s)s\tilde{P}(s)}$, the denominator is the same as before, one must just adapt the numerator of $\tilde{G}(s)$:

$$\begin{aligned} Num &= \tilde{A}(s)+\tilde{P}(s)+2sZ_s\tilde{A}(s)\tilde{P}(s) \\ &= \frac{T}{\sqrt{\frac{L'}{C'}}}\tilde{A}(p)+\frac{T}{\sqrt{\frac{L'}{C'}}}\tilde{P}(p)+2sZ_s\frac{T^2}{\frac{L'}{C'}}\tilde{A}(p)\tilde{P}p) \\ &= \frac{T}{\sqrt{\frac{L'}{C'}}}\left[\tilde{A}(p)+\tilde{P}(p)+2s(sL_s+R_s)\frac{T}{\sqrt{\frac{L'}{C'}}}\tilde{A}(p)\tilde{P}(p)\right] \\ &= \frac{T}{\sqrt{\frac{L'}{C'}}}\left[\tilde{A}(p)+\tilde{P}(p)+2\left(p^2\tau_a+p\rho_a\right)\tilde{A}(p)\tilde{P}p)\right]. \end{aligned}$$

Appendix C: Expression of the current in the switch

It was stated above that $I_s(s)=I_a(x=0,s)-I_p(x=0,s)$. The two contributions to the switch currents were also derived in the mathematical development leading to the transfer function $B(p)$:

$$\begin{aligned} I_a(x=0,s) =& \frac{u_0\left[A(s)-sZ_sA(s)P(s)\right]}{1-Z_s^2sA(s)sP(s)} \\ &+\frac{U_{out}^*\left[A(s)+sZ_sA(s)P(s)\right]}{1-Z_s^2sA(s)sP(s)}, \\ I_p(x=0,s) =& \frac{u_0\left[-P(s)+sZ_sA(s)P(s)\right]}{1-Z_s^2sA(s)sP(s)} \\ &+\frac{U_{out}^*\left[P(s)+sZ_sA(s)P(s)\right]}{1-Z_s^2sA(s)sP(s)}. \end{aligned}$$

Injecting $U_{out}^*=\frac{U_{out}}{sC'l}\left(\frac{1}{sL}+\frac{1}{Z}\right)=\frac{U_{out}}{2N}\frac{1}{sLC}$ (with the last simplification holding when there is no load connected at the output terminals of the generator) as well as assuming there is no resistance in the switch ($Z_s=sL_s$) leads to:

$$\begin{aligned} I_a(x=0,s) =& u_0\frac{\left[A(s)-s^2L_s^2A(s)P(s)\right]}{1-s^4L_s^2A(s)P(s)} \\ &+\frac{U_{out}}{2NsLC}\frac{\left[A(s)+s^2L_sA(s)P(s)\right]}{1-s^4L_sA(s)P(s)}, \\ I_p(x=0,s) =& u_0\frac{\left[-P(s)+s^2L_sA(s)P(s)\right]}{1-s^4L_s^2A(s)P(s)} \\ &+\frac{U_{out}}{2NsLC}\frac{\left[P(s)+s^2L_sA(s)P(s)\right]}{1-s^4L_s^2A(s)P(s)}. \end{aligned}$$

The final step is to inject the following expression of $U_{out}(s)$ which was also obtained previously:

$$U_{out}(s)=\frac{-su_0F(s)}{2NCs^2+\left(2NC-\frac{G(s)}{2N}\right)\left(\frac{s}{ZC}+\frac{1}{LC}\right)}.$$

This finally yields the following three expressions:

$$I_s(s)=\frac{u_0}{1-s^4L_s^2A(s)P(s)}\left[A(s)+P(s)-2s^2L_sA(s)P(s)-\frac{\frac{[A(s)-P(s)]^2}{1-s^4L_s^2A(s)P(s)}}{(2NC)^2\left(1+sLC\right)-\frac{A(s)+P(s)+2s^2L_sA(s)P(s)}{1-s^4L_s^2A(s)P(s)}}\right], \tag{C1}$$

$$I_a(x=0,s)=\frac{u_0}{1-s^4L_s^2A(s)P(s)}\left[A(s)-s^2L_sA(s)P(s)-\frac{\frac{[A(s)-P(s)]\left[A(s)+s^2L_sA(s)P(s)\right]}{1-s^4L_s^2A(s)P(s)}}{(2NC)^2\left(1+sLC\right)-\frac{A(s)+P(s)+2s^2L_sA(s)P(s)}{1-s^4L_s^2A(s)P(s)}}\right], \tag{C2}$$

$$I_p(x=0,s)=\frac{u_0}{1-s^4L_s^2A(s)P(s)}\left[-P(s)+s^2L_sA(s)P(s)-\frac{\frac{[A(s)-P(s)][P(s)+sL_sA(s)P(s)]}{1-s^4L_s^2A(s)P(s)}}{(2NC)^2\left(1+sLC\right)-\frac{A(s)+P(s)+2s^2L_sA(s)P(s)}{1-s^4L_s^2A(s)P(s)}}\right]. \tag{C3}$$

To consider resistive losses in the conductors, one can simply replace $A(s)$ by $\tilde{A}(s)$ and $P(s)$ by $\tilde{P}(s)$.

Performing a similar mathematical development with the boundary conditions used by Bichenkov *et al.* leads to the following three expressions:

$$I_s(s)=u_0\left[A(s)+P(s)-\frac{[A(s)-P(s)]^2}{(2NC)^2\left(1+sLC\right)-A(s)+P(s)}\right], \tag{C4}$$

$$I_s(s)=u_0\left[A(s)-\frac{[A(s)-P(s)]A(s)}{(2NC)^2\left(1+sLC\right)-A(s)+P(s)}\right], \tag{C5}$$

$$I_s(s) = u_0 \left[-P(s) - \frac{[A(s) - P(s)]\, P(s)}{(2NC)^2 (1 + sLC) - A(s) + P(s)} \right]. \tag{C6}$$

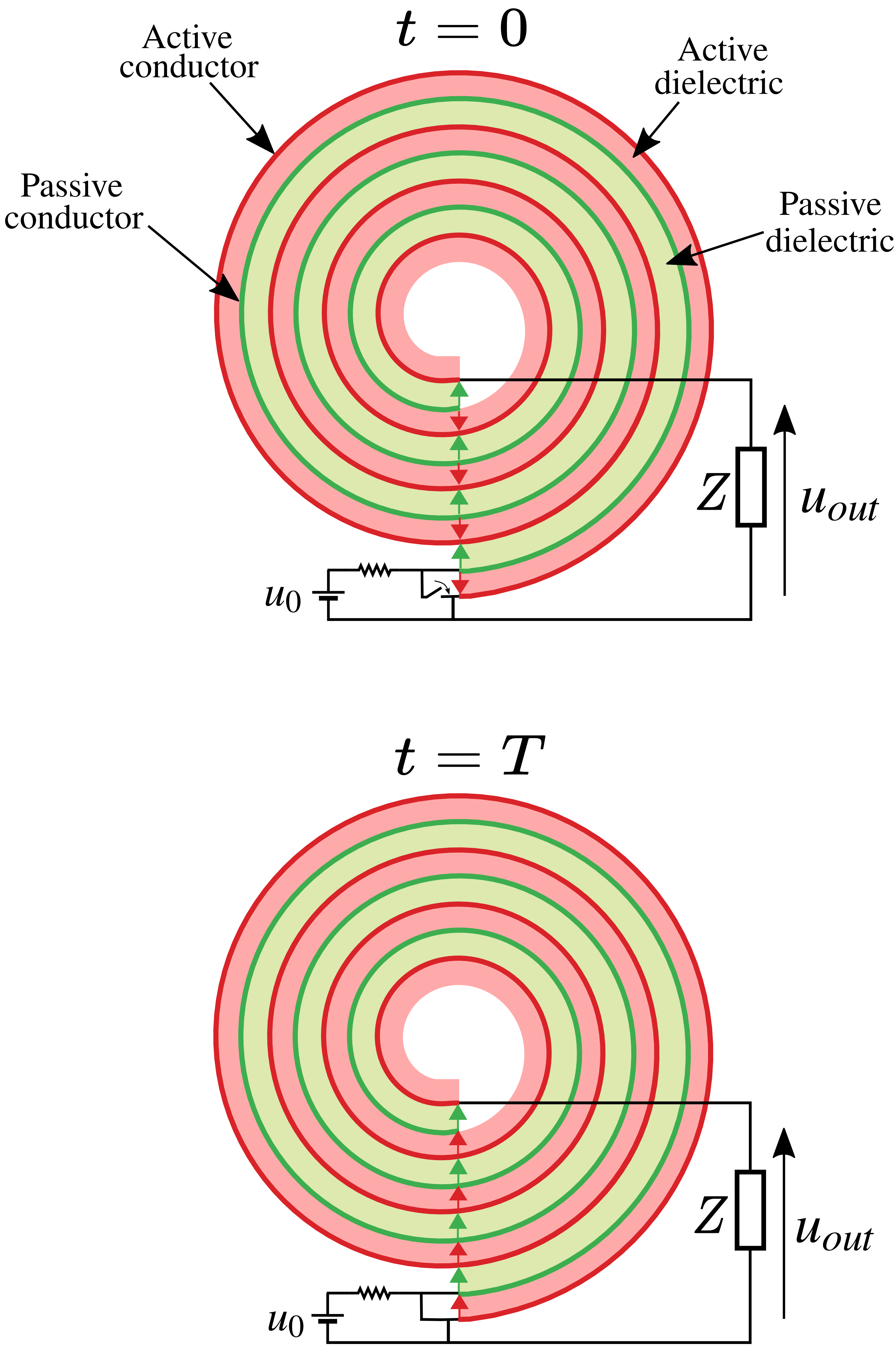
$t = 0$
Active conductor
Active dielectric
Passive conductor
Passive dielectric
Z
u_{out}
u_0
$t = T$
Z
u_{out}
u_0

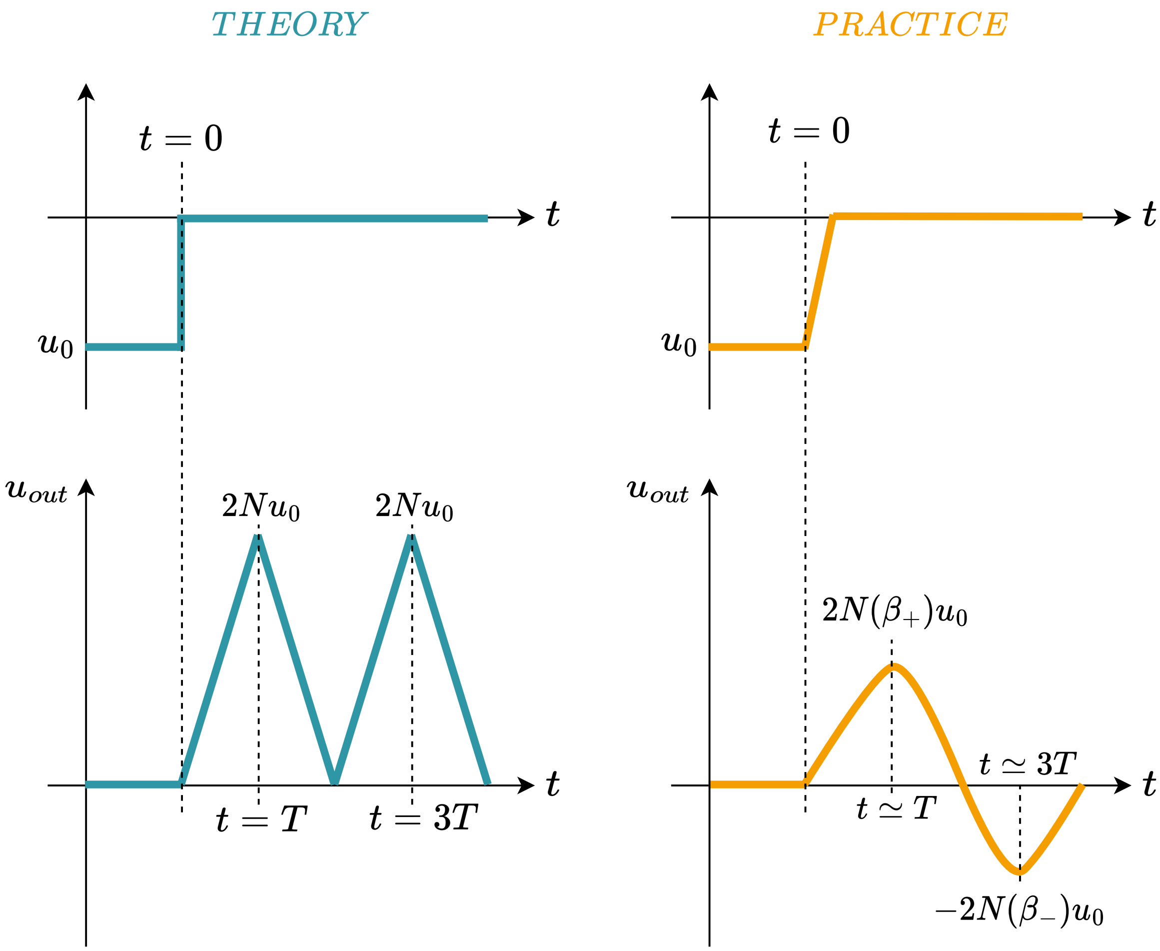
THEORY
PRACTICE
$t = 0$
t
u_0
u_{out}
$2Nu_0$
$2Nu_0$
$t = T$
$t = 3T$
$t = 0$
t
u_0
u_{out}
$2N(\beta_+)u_0$
$t \simeq 3T$
$t \simeq T$
$-2N(\beta_-)u_0$

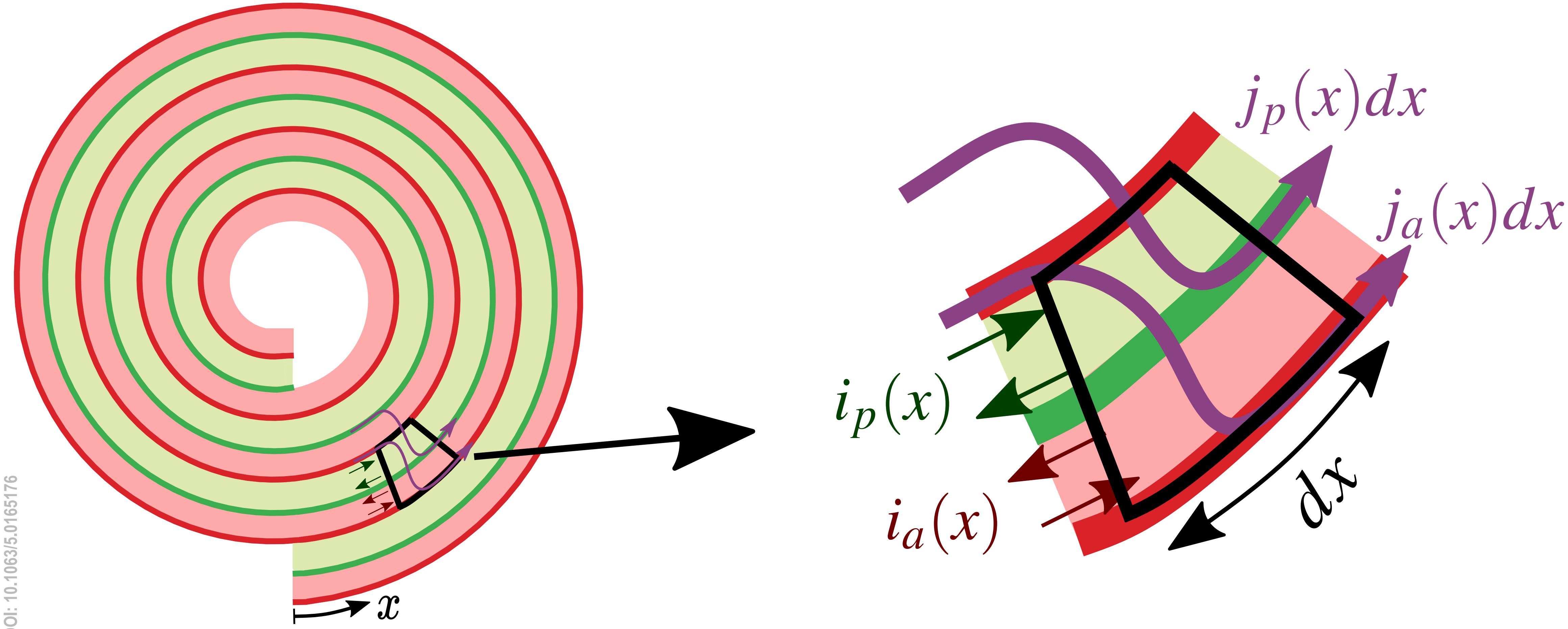
x
$j_p(x)dx$
$j_a(x)dx$
$i_p(x)$
$i_a(x)$
dx

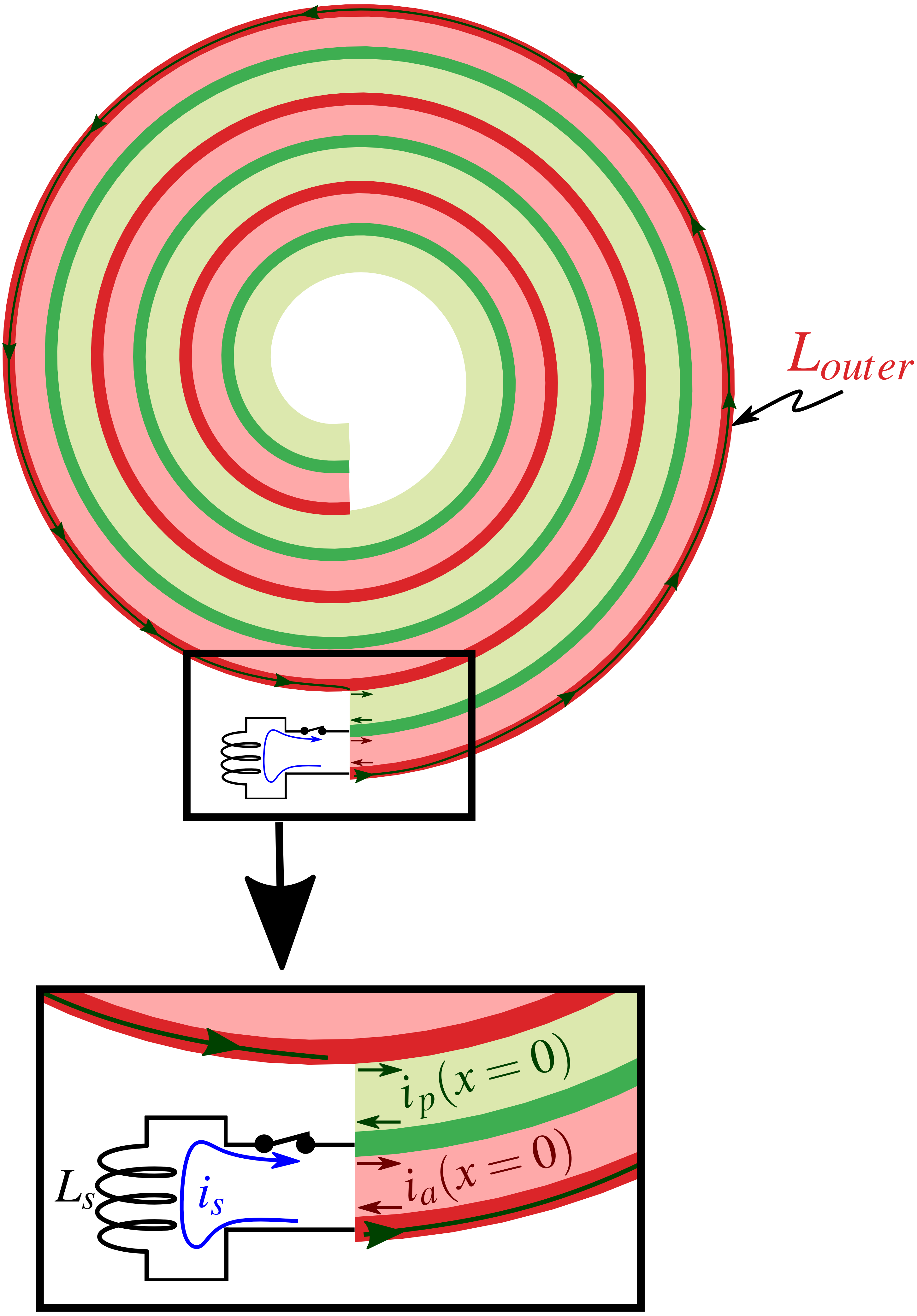
L_{outer}
$i_p(x=0)$
$i_a(x=0)$
L_s
i_s


Output voltage measurement
Height:
$w = 25.4$ mm
u_0 connections
Mean diameter: $D = 70$ mm

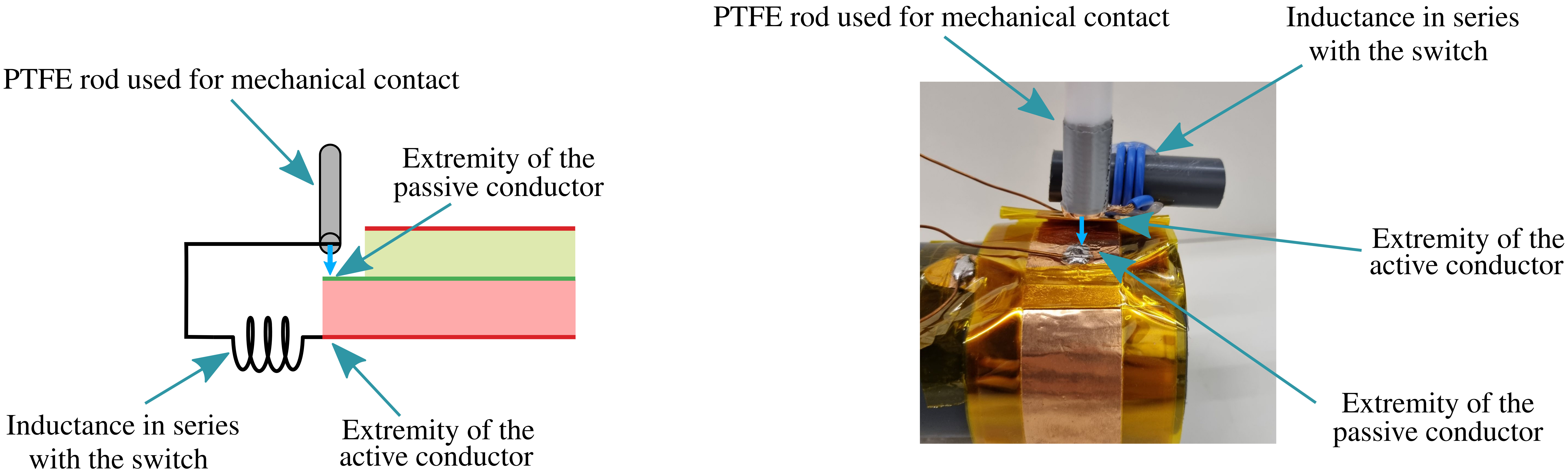
PTFE rod used for mechanical contact
Extremity of the passive conductor
Inductance in series with the switch
Extremity of the active conductor
PTFE rod used for mechanical contact
Inductance in series with the switch
Extremity of the active conductor
Extremity of the passive conductor

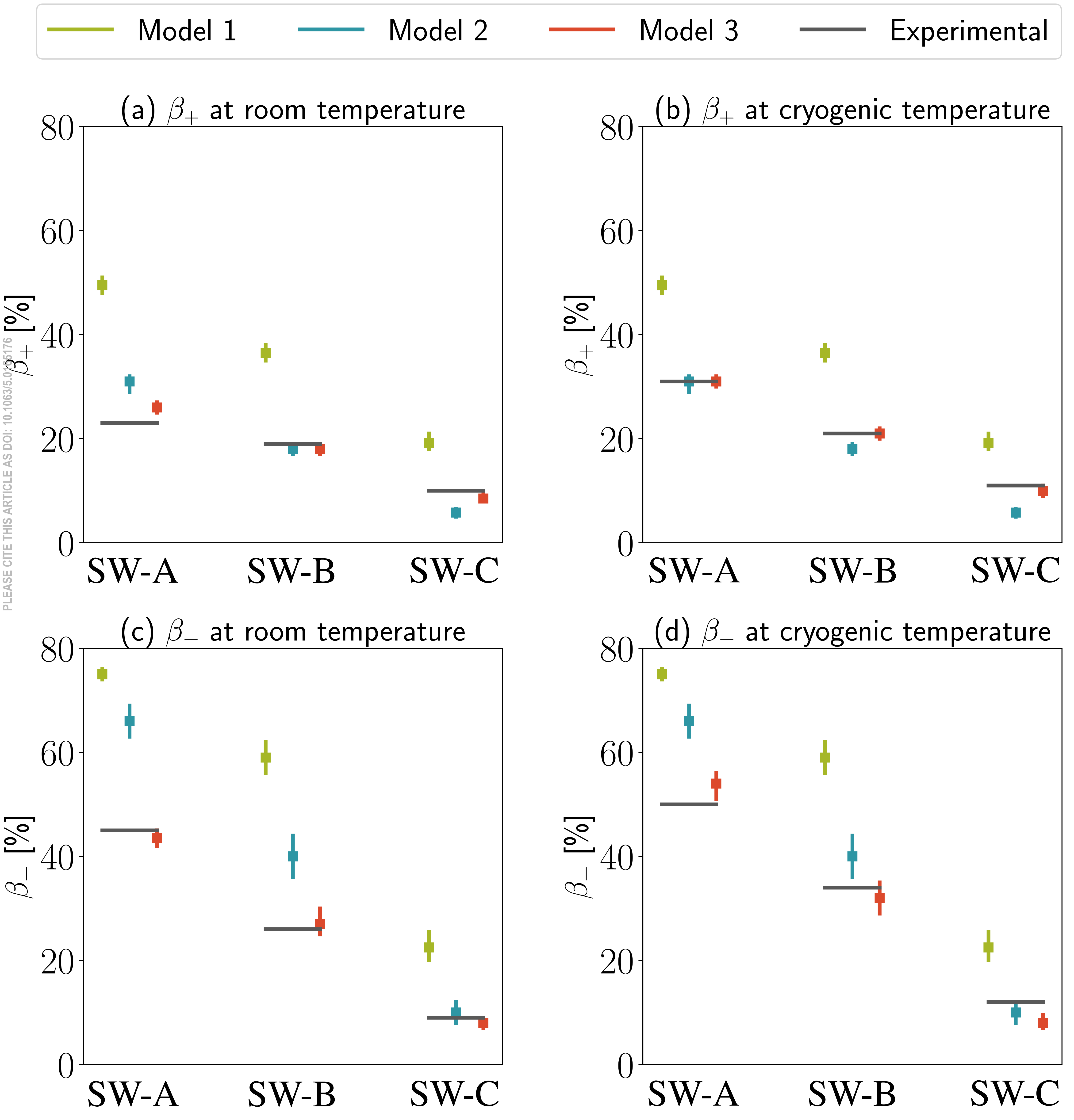
Model 1
Model 2
Model 3
Experimental
(a) β_+ at room temperature
(b) β_+ at cryogenic temperature
(c) β_- at room temperature
(d) β_- at cryogenic temperature
β_+ [%]
β_- [%]
0
20
40
60
80
SW-A
SW-B
SW-C

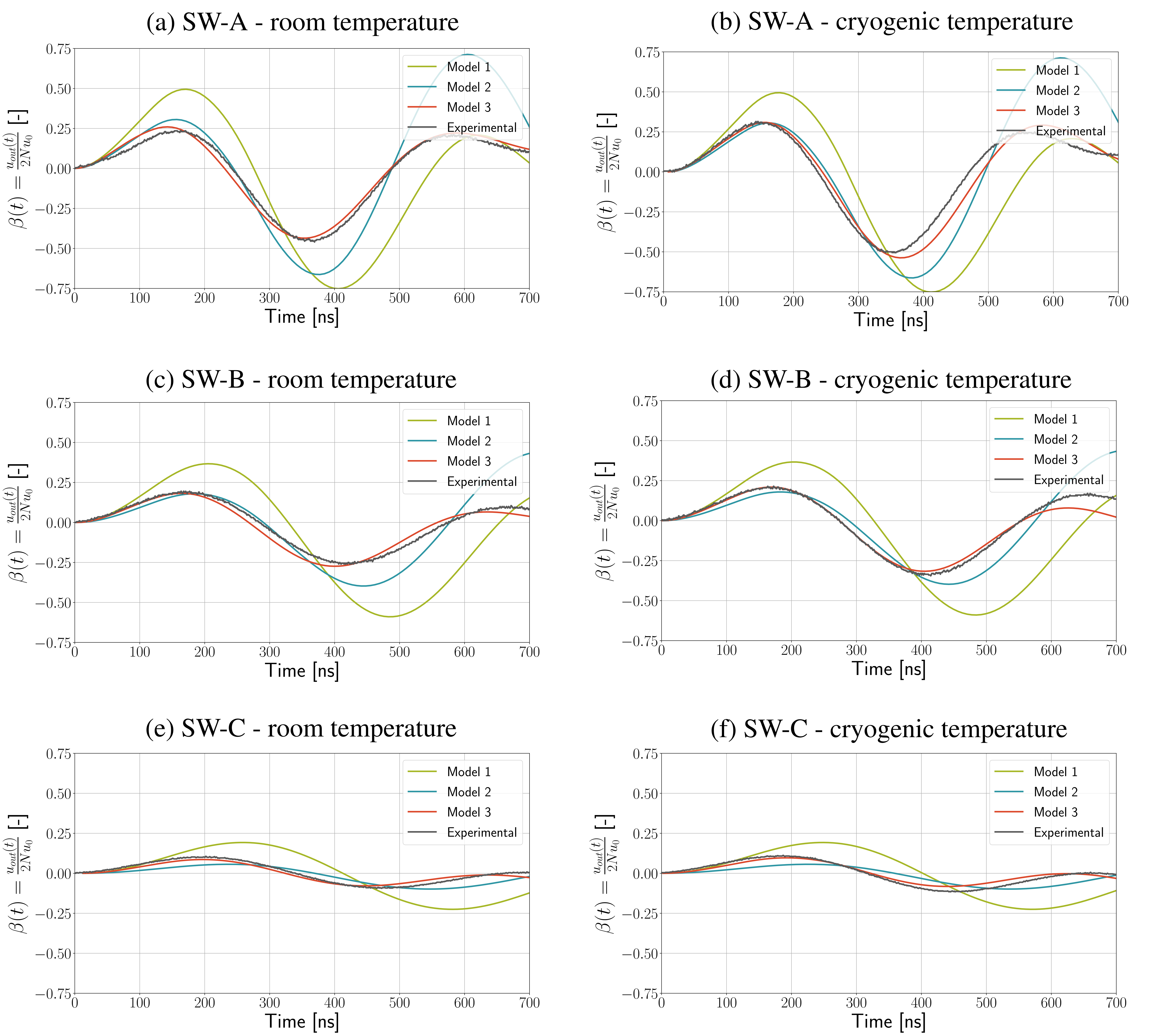
(a) SW-A - room temperature
(b) SW-A - cryogenic temperature
(c) SW-B - room temperature
(d) SW-B - cryogenic temperature
(e) SW-C - room temperature
(f) SW-C - cryogenic temperature
Model 1
Model 2
Model 3
Experimental
$\beta(t) = \frac{u_{out}(t)}{2Nu_0}$ [-]
Time [ns]
0.75
0.50
0.25
0.00
−0.25
−0.50
−0.75
0
100
200
300
400
500
600
700

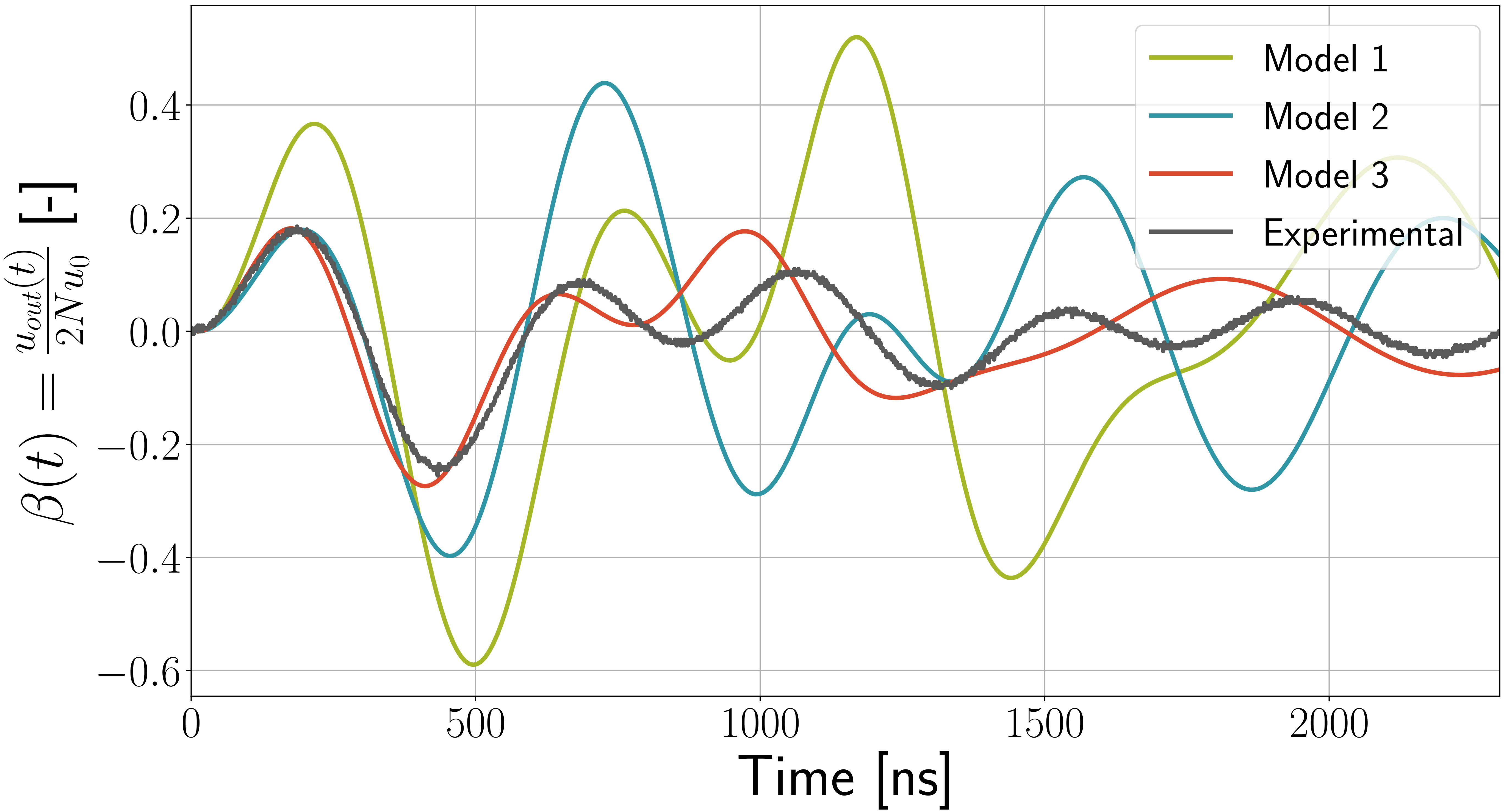

Model 1
Model 2
Model 3
Experimental
$\beta(t) = \frac{u_{out}(t)}{2Nu_0}$ [-]
Time [ns]
0.4
0.2
0.0
−0.2
−0.4
−0.6
0
500
1000
1500
2000

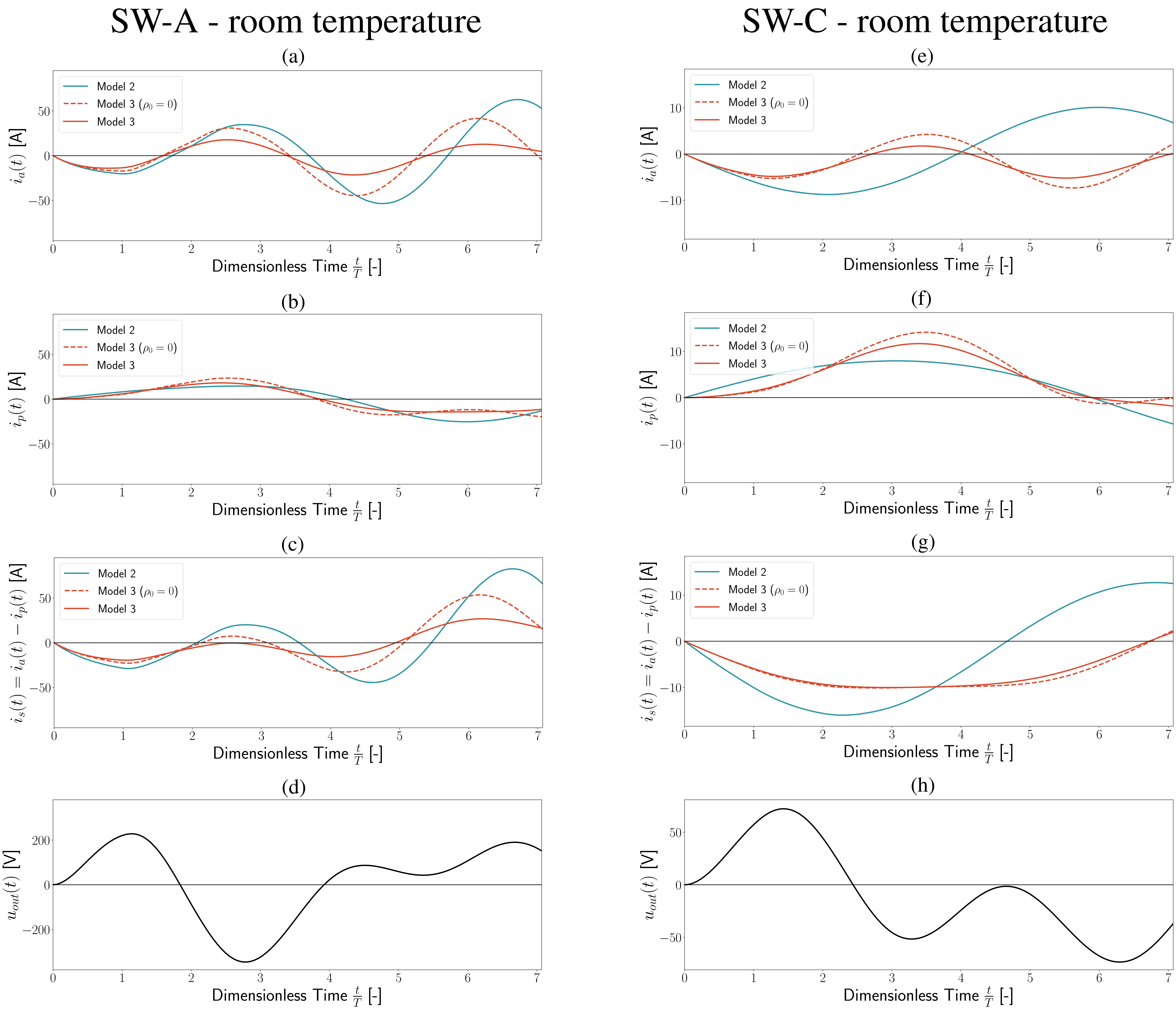
SW-A - room temperature
SW-C - room temperature
(a)
(b)
(c)
(d)
(e)
(f)
(g)
(h)
Model 2
Model 3 ($\rho_0 = 0$)
Model 3
$i_a(t)$ [A]
$i_p(t)$ [A]
$i_s(t) = i_a(t) - i_p(t)$ [A]
$u_{out}(t)$ [V]
Dimensionless Time $\frac{t}{T}$ [-]

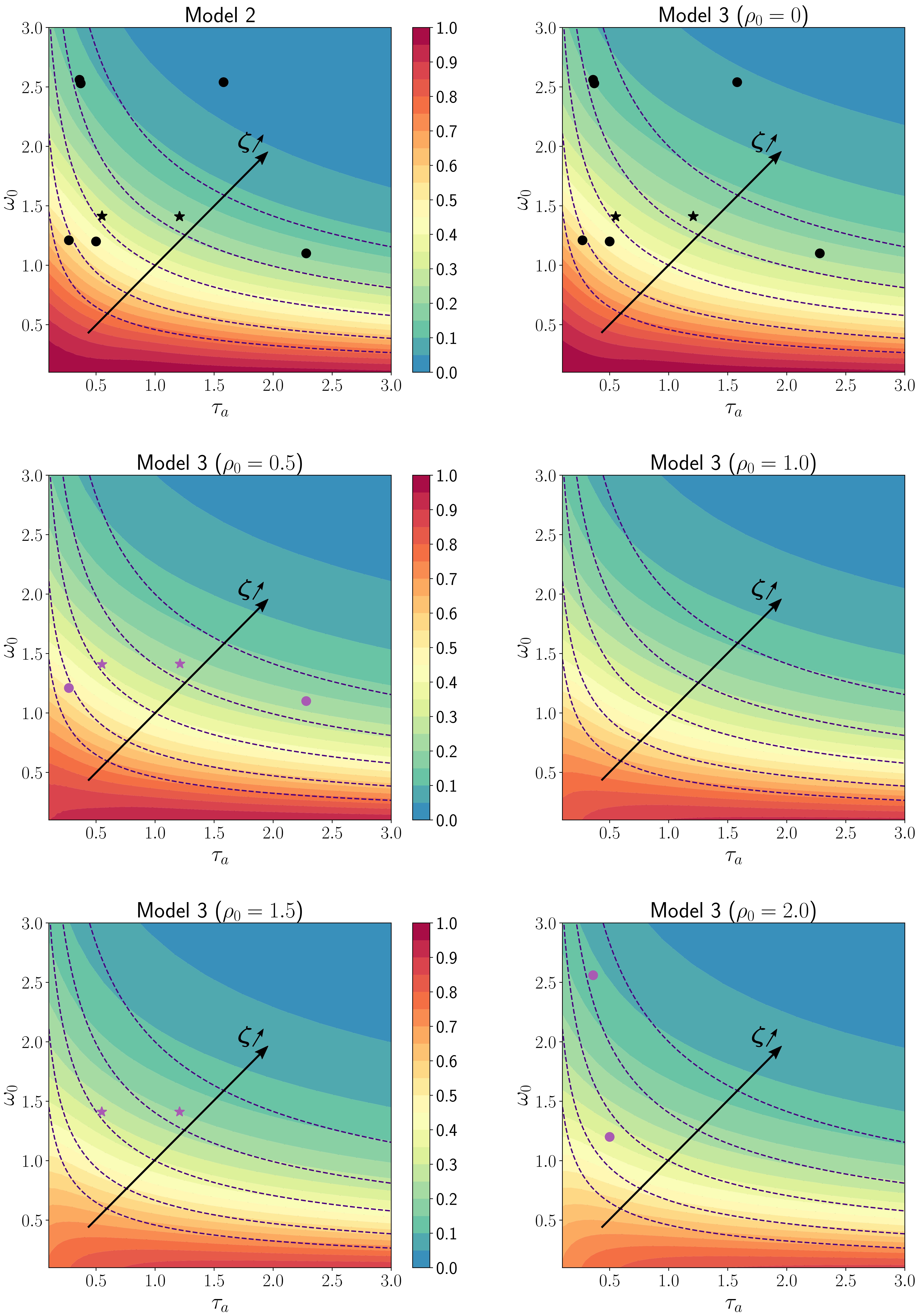
Model 2
Model 3 ($\rho_0 = 0$)
Model 3 ($\rho_0 = 0.5$)
Model 3 ($\rho_0 = 1.0$)
Model 3 ($\rho_0 = 1.5$)
Model 3 ($\rho_0 = 2.0$)
ω_0
τ_a
$\zeta \nearrow$

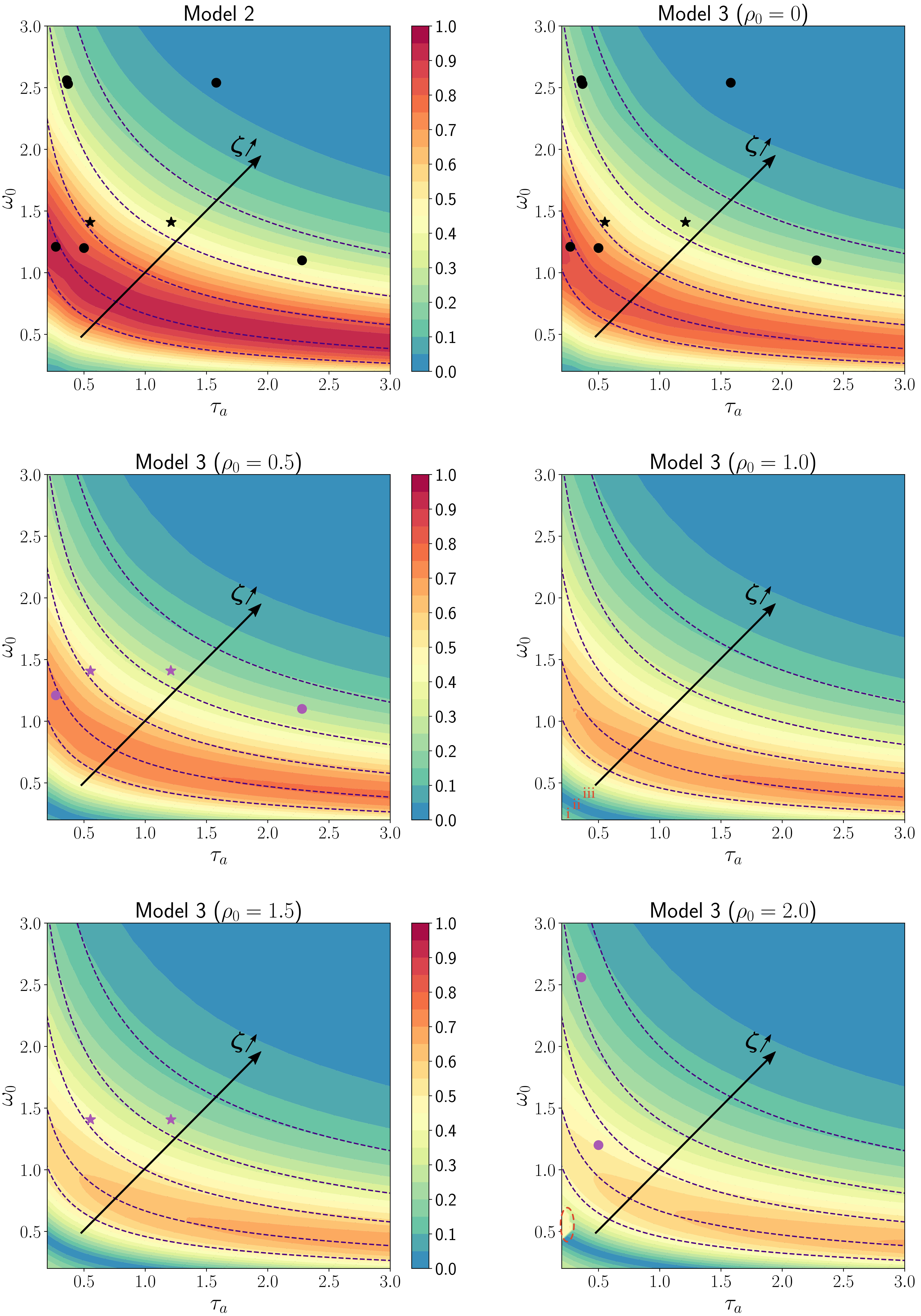
Model 2
Model 3 ($\rho_0 = 0$)
Model 3 ($\rho_0 = 0.5$)
Model 3 ($\rho_0 = 1.0$)
Model 3 ($\rho_0 = 1.5$)
Model 3 ($\rho_0 = 2.0$)
ω_0
τ_a
$\zeta \nearrow$
i
ii
iii

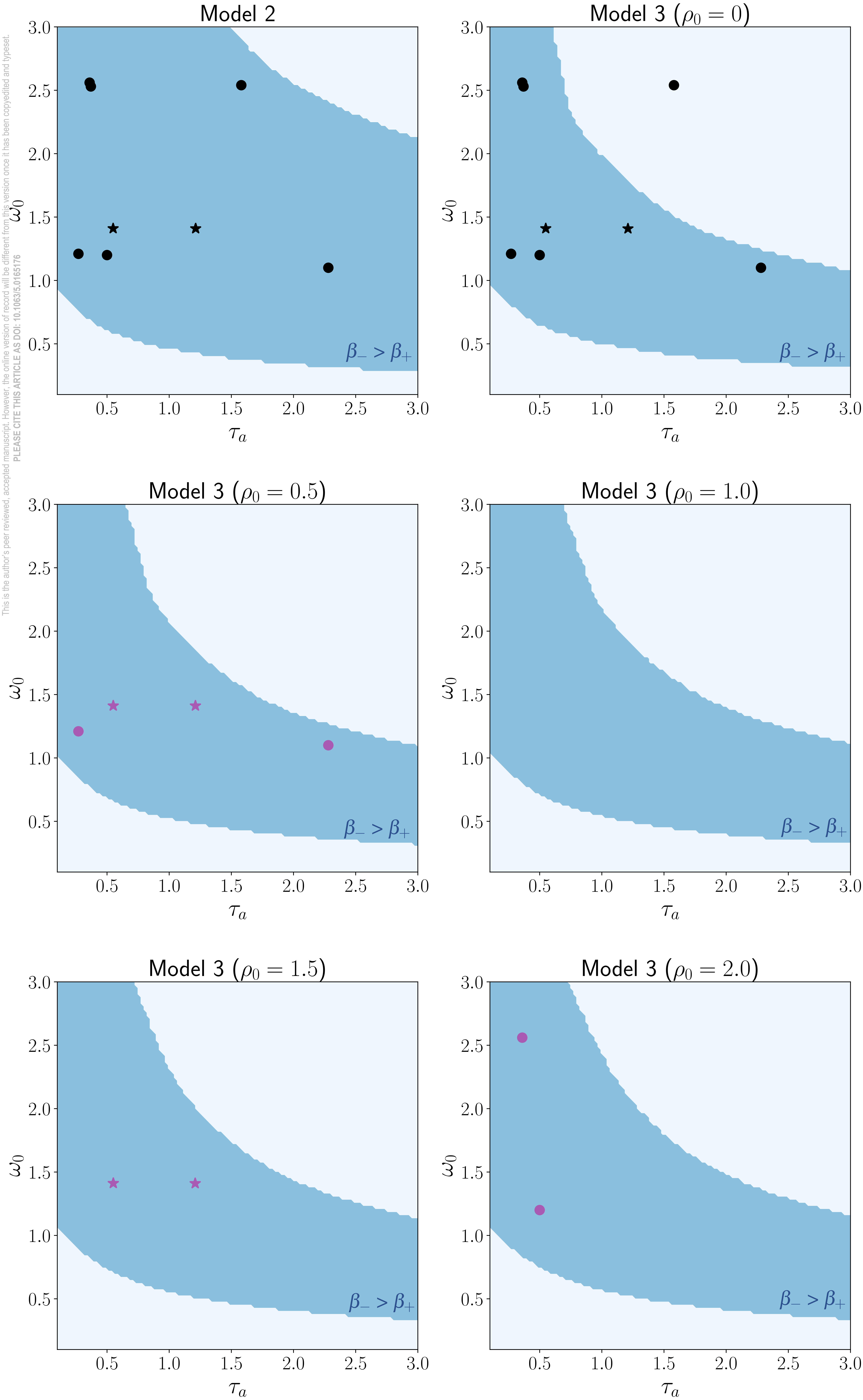
Model 2
Model 3 ($\rho_0 = 0$)
Model 3 ($\rho_0 = 0.5$)
Model 3 ($\rho_0 = 1.0$)
Model 3 ($\rho_0 = 1.5$)
Model 3 ($\rho_0 = 2.0$)
ω_0
τ_a
$\beta_- > \beta_+$

(a)

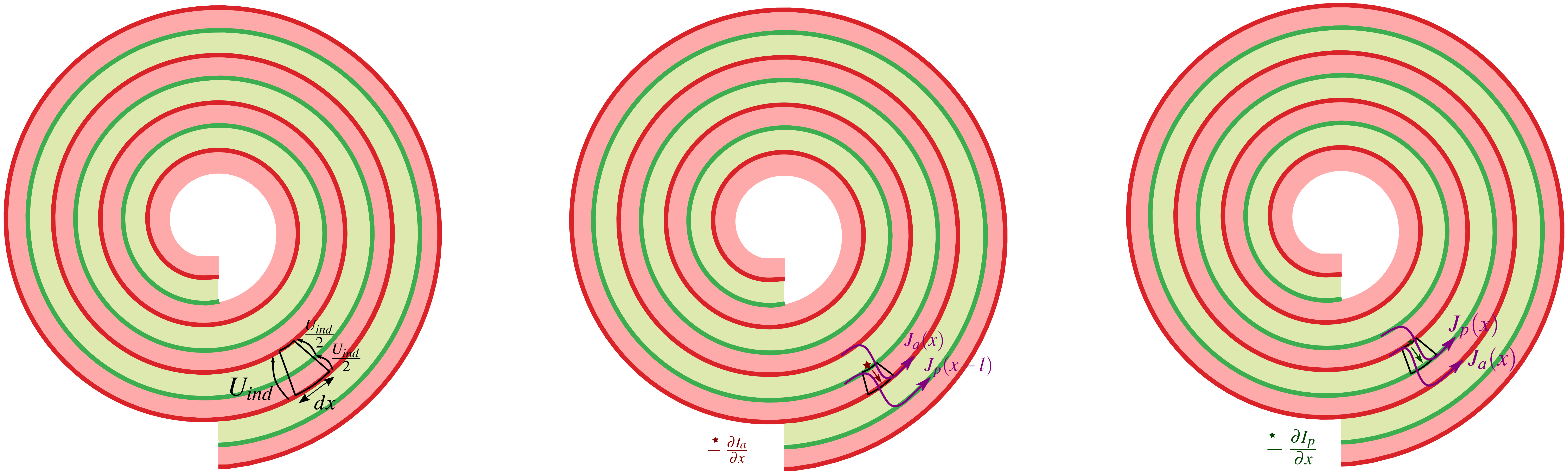
$\frac{U_{ind}}{2}$
$\frac{U_{ind}}{2}$
U_{ind}
dx
$J_a(x)$
$J_p(x-l)$
$-\frac{\partial I_a}{\partial x}$
$J_p(x)$
$J_a(x)$
$-\frac{\partial I_p}{\partial x}$

(b)

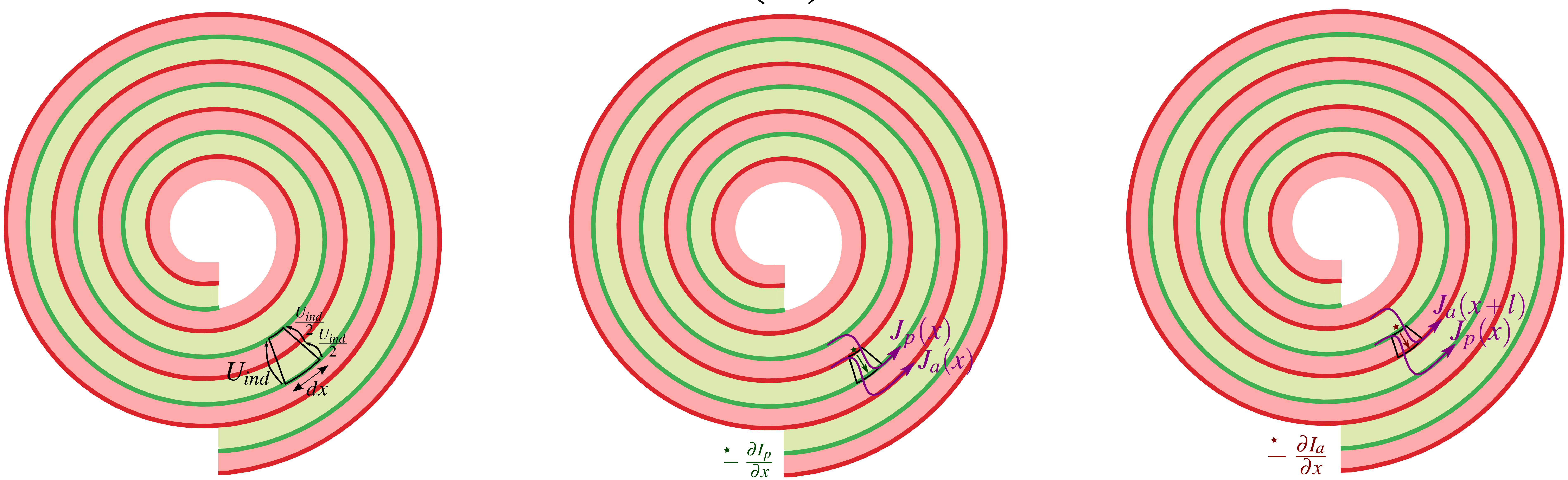
$\frac{U_{ind}}{2}$
$\frac{U_{ind}}{2}$
U_{ind}
dx
$J_p(x)$
$J_a(x)$
$-\frac{\partial I_p}{\partial x}$
$J_a(x+l)$
$J_p(x)$
$-\frac{\partial I_a}{\partial x}$